

The Starburst – AGN Connection II: The Nature of Luminous Far Infrared Galaxies as Revealed by **VLBI**, Radio, Infrared and Optical Observations

HARDING E. SMITH ^{1,2}

Center for Astrophysics and Space Sciences

and

Department of Physics,

University of California, San Diego

La Jolla, CA 92093-0424;

hsmith@ucsd.edu

COLIN J. LONSDALE ²

Haystack Observatory,

Massachusetts Institute of Technology

Off Route 40

Westford, MA 01886;

cjl@wells.haystack.edu

CAROL J. LONSDALE ²

Infrared Processing and Analysis Center

California Institute of Technology 100-22

Pasadena, CA 91125;

cjl@ipac.caltech.edu

Subject headings: galaxies: active — infrared: galaxies --- radio continuum: galaxies

Received _____; accepted _____

¹ also, Infrared Processing and Analysis Center, California Institute of Technology

²Visiting Observer at the VLA of the National Radio Astronomy Observatory which is operated by Associated Universities, Inc. under contract with the National Science Foundation.

ABSTRACT

We present here detailed results of an 18 cm VLBI survey of 31 luminous ($L_{\text{FIR}} > 10^{11.25} L_{\odot}$), radio-compact ($\theta \leq 0''.25$) infrared galaxies (LFIRGs). High-resolution VLA maps at 15 and 22GHz are presented for 14 of these galaxies which exhibit compact milliarcsecond scale emission, providing information about radio structure of LFIRGs on scales from $0''.004$ to $1''.0$. We also present new optical spectrophotometric observations. Over half the sample galaxies show high-brightness temperature radio emission from the VLBI data, with $T_b > 10^5 \text{K}$ and structure on **scales** of 5 – 150 mas, as previously reported in Lonsdale, Smith and Lonsdale (1993). The median VLBI power for detected **sources** is $\log P_{\text{vlbi}} = 22.0 (WHz^{-1})$, and the mean ratio of VLBI to total 1.6 GHz flux density $\langle S_{\text{vlbi}}/S_{\text{total}} \rangle = 0.12$. Further structure is observed on the larger VLA scales. No highly-significant ($P < 1\%$) statistical correlations are found between the presence or strength of the VLBI emission and other observed quantities, including total radio power, radio spectral index, FIR luminosity and colors, radio-infrared ratio, molecular gas mass, and optical excitation. Statistical analysis does suggest that the infrared luminosity, molecular gas emission and radio emission on VLA and VLBI scales are physically related.

Previous work (Lonsdale, Smith and Lonsdale 1995) demonstrated that hidden (dust-enshrouded) AGN are *capable* of powering LFIRGs and giving rise to the observed VLBI and VLA scale structures; here we investigate the complementary question of whether a starburst can completely explain the observed characteristics, including the high brightness temperature radio emission. Simple Starburst models show that the far-infrared luminosity can be explained by starbursts in all cases except Mkn 231, although for some objects the constraints imposed on the initial mass function are severe. Using our Starburst models we model the VLBI data for 11 galaxies with detailed radio structural information using complexes of radio supernovae. The required supernova rates are $\nu_{sn} \sim 0.1\text{-}2 \text{ yr}^{-1}$, consistent with the rates derived from the Starburst

model to explain the observed far-infrared luminosities. However *in all cases we* require complexes of extremely luminous radio supernovae to **explain the high T_b emission**. In some cases the RSN must have implausibly high radio powers, more than an order of magnitude larger than any previously reported RSN; in our view **these** sources represent AGN radio cores.. In most cases an acceptable fit requires that the RSN be clumped on **pc-scales**. Within a given clump, multiple RSN must detonate within time-scales of a few years. Based on this analysis we conclude that 7/11 systems can be plausibly explained as Starbursts. Four galaxies, UGC 2369, Mrk 231, UGC 5101 and NGC 7469, almost certainly house AGN radio **cores**. From our **modelling**, coupled with other recent VLBI and infrared evidence, we conclude that Arp 220 is dominated by a massive Starburst at radio and infrared wavelengths.

1. INTRODUCTION

Luminous Far-Infrared Galaxies (**LFIRGs**), are characterized by extreme luminosities ($L \gtrsim 10^{11} L_{\odot}$) at mid – far-infrared wavelengths. Typically the far-infrared luminosity of **LFIRGs** exceeds the UV-optical radiation by an order of magnitude or more. At the most luminous end of the luminosity function ($L_{FIR} \gtrsim 10^{12} L_{\odot}, H = 75 \text{ km s}^{-1} \text{ Mpc}^{-1}$), **LFIRGs** may be the dominant galaxy population, outnumbering UV/optically-selected and radio-selected QSOS (Soifer *et al.* 1989). In the most luminous **LFIRGs** the activity is highly concentrated towards the central few hundred parsecs, as shown by high resolution VLA mapping in the radio continuum (Condon *et al.* 1991, **CHYT**), and high resolution molecular line studies which show extremely high nuclear column densities, reaching $N_H = 10^{24} \text{ cm}^{-2}$ for Arp 220 (Scoville *et al.* 1991). A large fraction of **LFIRGs** are interacting or merger systems, and the fraction increases with luminosity (Sanders *et al.* 1988). At the highest luminosities essentially all **LFIRGs** are involved in advanced merger episodes. There is a consensus that **LFIRGs** are undergoing transient episodes, triggered when gaseous material is channeled into the central regions by the interaction event to feed either a nuclear starburst, a central compact object, or both (see Sanders & Mirabel 1996 for an excellent review). We seek to understand two fundamental questions:

- What is the nature of the dominant energy source in **LFIRGs**?
- What is the relationship between AGN and Starburst activity in those systems in which the two phenomena coexist?

CHYT and others have argued that the FIR luminosity and the radio continuum properties of these galaxies can be explained by very compact nuclear starburst events. Sanders *et al.* (1988), on the other hand, have concluded that **LFIRGs** are likely to be harboring dust-enshrouded AGN which are responsible for their far-infrared emission, based on the similar space densities of **LFIRGs** and AGN, and the fact that there is a trend amongst **LFIRGs** that the most luminous show the strongest evidence for AGN activity in their optical spectroscopic characteristics. Sanders *et al.* proposed an evolutionary sequence in which **LFIRGs** will evolve into optically- dominated

AGN when the central concentration of dusty molecular material is blown away by the developing compact object, and attributed the FIR emission to a warped disk. Another possibility is that in the currently popular AGN unification models featuring a thick molecular torus, **LFIRGs** are the same population as FIR-luminous optically-selected AGN but viewed edge-on to the disk so that the active nucleus is obscured, and the **FIR** emission is due to a centrally heated torus (Pier & Krolik 1992, 1993, Granato & Danese 1994, Granato, Danese & Francheschini 1996). In the model of Rowan-Robinson (1995) **LFIRGs** are composite objects in which a nuclear starburst is responsible for the longer wavelength ($\lambda \gtrsim 30 \mu\text{m}$) emission, and in 10-20% of **LFIRGs** an AGN is also present and is responsible for additional mid-infrared (10-30 μm) emission.

Lonsdale, Lonsdale and Smith (1992; **LLS92**) and Lonsdale, Smith and Lonsdale (1993; Paper I), have addressed the question of what fraction of **LFIRGs** possess a possible dust-obscured classical AGN using cm-wavelength radio continuum observations with global very-long-baseline arrays to penetrate the shroud of dust surrounding the nuclear energy source and to scrutinize them with milli-arcsecond resolution. Given the large columns of dense material found in these galaxies ($N_H = 10^{21} - 10^{24} \text{cm}^{-2}$), only long-wavelength radio or hard X-ray photons may penetrate the material along the line-of-sight. The detection of high-brightness-temperature, milli-arcsecond VLBI emission was considered strong evidence for the presence of a classical AGN. In a pilot 18-cm VLBI search (**LLS92**) the efficacy of this technique was demonstrated in the detection of milli-arcsecond-scale VLBI emission in 3/5 infrared-bright galaxies, including the peculiar compact radio source Mrk 297A. This source provided a caution for interpretation of compact, high- T_b emission as it may represent the extreme member of a new class of exceptionally luminous radio supernovae (Yin & Heeschen 1991, **LLS92**, Wilkinson & de Bruyn 1990), which may be common in Starburst galaxies and may mimic the radio properties of low-power AGN radio cores.

In 1991, September, we employed a global VLBI array at 18cm to survey 31 compact, luminous infrared galaxies from the IRAS Bright Galaxy Sample (**BGS**; Soifer *et al.* 1989) which comprise part of a complete sample of 40 Luminous **FIR** Galaxies observed at 8.44GHz with the VLA by CHYT. The detection results from this survey were presented in Paper 1: 17/31 galaxies show

high brightness-temperature emission with $T_b \geq 10^6 K$ which according to our axiom indicates the possible presence of an AGN core. Since this was a detection rather than an imaging experiment, full synthesized maps were not available. Our conclusion was that it is likely that most, possibly all, of the most luminous FIR galaxies possess compact **high- T_b** radio emission. These were interpreted as obscured AGN with a proviso that in some cases starburst-generated supernovae may be responsible for some or all of high brightness temperature emission.

Norris *et al.* (1990) have performed a similar experiment, using the Parkes-Tidbinbilla Interferometer to survey an equatorial/southern sample of infrared galaxies, concluding that **high- T_b** cores are present only in high-excitation (**Seyfert**) infrared galaxies. Their experiment differs from ours in three principal respects: 1) The 275km baseline of the PTI gives them a principal sensitivity to structure on scales of order **0".1 at 18cm**, whereas the **VLBI** baselines employed here give us sensitivity to structures down to a few **milliarcseconds**, 2) our experiment has a lower flux-density limit; most of the sources detected in our study would fall below their sensitivity limit, and 3) their sample reaches to much lower FIR luminosity, **$\log L_{FIR} < 10(LO)$** , with fewer than a quarter of their systems falling above our lower luminosity cutoff. Their somewhat different conclusions can be understood in light of their different sample selection criteria and **T_b** sensitivity. For three galaxies in common (UGC 2369, NGC 2623 and NGC 7469), both surveys report detections at similar 18cm flux density.

In a related work (Lonsdale, Smith and Lonsdale 1995 — **LSL95**), we posed the question: “If **LFIRGs** possess an AGN core, is that AGN capable of powering the observed FIR luminosity?” We compared the **bolometric** output of **LFIRGs** to that of radio-quiet QSOS of comparable radio core power, demonstrating that the milliarcsecond **VLBI** structures in Luminous FIR Galaxies follow a common relation between compact radio power and **bolometric** luminosity with radio-quiet AGN in the Palomar-Green Bright Quasar Sample (**BQS**; Schmidt & Green 1983). Therefore, if they do possess a buried core, similar to that of RQQs, the obscured QSO is *capable* of generating the observed FIR luminosity. This result does not prove that a hidden QSO does provide a significant fraction of the observed far-infrared emission, however, nor does it rule out the presence of a

starburst as well. Indeed, the VLBI-detected structure represents **only 5–10%** of the total nuclear centimeter radio continuum emission in **LFIRGs**, and the origin of this emission, extended on scales of a few hundred pc, would still be uncertain even if the **VLBI-scale** emission is produced by AGN activity.

One of the most intriguing, and unexpected, results from this effort has been the detection of strong parsec-scale OH-maser emission in Arp 220, the prototype Luminous Far-Infrared Galaxy and Megamaser (Lonsdale *et al.* 1994), implying that the bulk of **megamaser** emission in Arp 220 originates on scales of order **10pc**. We interpreted the compact OH masers as amplification of the VLBI core by a molecular region in Arp 220 which shares many characteristics in common with the putative molecular torus which distinguishes broad-line from narrow-line AGN in unified AGN models. The pumping mechanism for the OH molecules has generally been ascribed to the high FIR (55–120 μ m) photon density which would then imply a very compact, luminous central infrared source, further strengthening the case for the presence of a central engine. However, recent VLBI maser imaging experiments have shown that, while the bulk of maser emission in Arp 220 and **IIIZw35** is indeed compact, the emission is concentrated in a series of structures which are spatially unrelated to the compact continuum (Lonsdale *et al.* 1997, Diamond *et al.* 1997).

In the present paper we present new high resolution 15 and 22GHz VLA A array imaging observations of 14 sources. Our goal is to study the connection between the compact VLBI components and the more diffuse emission seen in the 0! '25 resolution studies of CHYT and further elucidate the relative importance of starburst and AGN emission. We also report full details of the **VLBI** survey observations of 31 luminous FIR galaxies presented in Paper I, and combine the high frequency VLA data with the VLBI data to derive a picture of the radio continuum structure from 4 **milliarcseconds** to 1 **arcsecond**. We compare the radio continuum structure and power present on the various size scales to that expected for a starburst-supernova model and to AGN. In addition, we present new optical spectrophotometry of sample galaxies which, combined with data from the literature, allow quantitative excitation measures to be obtained for the entire sample. These data are combined with other data from the literature to examine the relationships between the VLBI

compact structure and other radio, infrared and optical characteristic.

In Section 2 we describe our **LFIRG** sample selection, and in Section 3 we describe the new high resolution VLA observations, and provide full details of the 18cm **VLBI** sample of Paper 1. We also present the available literature data. Section 3.3 describes our new optical spectrophotometry. We discuss the implications of the combined dataset for the nature of **LFIRGs** in Section 4. In Section 4.1 we investigate statistical relationships among **VLBI**, **VLA-scale** radio, infrared and optical characteristics using survival analysis techniques, as appropriate for this censored data set. In Section 4.2 we describe simple model **starburst** calculations which we employ for further discussion of the radio structure in **LFIRGs**. Section 4.3 we present the starburst and AGN models for the radio continuum visibility functions. Our conclusions are presented in Section 5.

2. THE LUMINOUS FIR GALAXY SAMPLE

A complete sample of the 40 most luminous members of the IRAS Bright Galaxy Sample (BGS; Soifer *et al.* 1989) with $S_{60\mu m} > 5.24 \text{ Jy}$, such that $\log [L_{FIR}/L_{\odot}] > 11.25$, was constructed by CHYT for observation with the VLA-A array at 8.4GHz. The observations were made with angular resolution typically about $0.''25$ and **r.m.s.** background noise levels of approximately 0.03 mJy. These Luminous FIR Galaxies are, as a class, extremely compact: most of the 8.4GHz images show nuclear features of angular extent comparable to or smaller than the 0.25 arcsecond restoring beam.” The extreme compactness implied by the **deconvolved** sizes calculated by CHYT are of considerable significance to the interpretation of Luminous FIR galaxies as Starbursts. CHYT model these systems as luminous starbursts with thermal dust emission at $T \approx 60 - 80 \text{ K}$ which are so dense as to be optically thick to free-free absorption at 1.5GHz and to dust extinction at $25\mu m$.

We list the galaxies from the CHYT **LFIRG** Sample in Table 1. In Column 1 is the system name from the catalog which we have deemed to be most common usage, Columns 2 and 3 list the 1950 radio positions of radio components associated with each system. The positions generally refer to compact 8.4GHz components detected by CHYT and considered as possible VLBI targets,

with the exception of NGC 1614 where the **1.49GHz** position is taken from Condon *et al.* (1990). Note that the individual components for multiple sources are listed not in the conventional RA order, but **rather** in order of estimated maximum **VLBI** flux density — VLBI detectability (see §2.1 below). Columns 4-12 list respectively, the system distance, assuming $H_0 = 75 \text{ km s}^{-1} \text{ Mpc}^{-1}$, the molecular gas mass, M_{H_2} , principally from CO observations by Sanders, Scoville and Soifer (1991), FIR luminosity and IRAS flux densities from Soifer *et al.* (1989), and 1.5GHz radio flux density and 1.5–8.4GHz spectral index from CHYT.

2.1. The VLBI **Subsample**

Although CHYT were able to resolve nearly all of the nuclear features at 8.4GHz, deriving deconvolved sizes by assuming elliptical gaussian brightness distributions, the degree of resolution is typically small, and the data are generally consistent with a large fraction of the flux density in these features originating in regions much smaller than the deconvolved gaussian sizes quoted. This suggests that the CHYT sample is an ideal sample for investigation with VLBI techniques. In order to estimate the prospects of success and to create a **subsample** for actual observation, we calculated for each source the maximum possible 18cm flux density present on scales smaller than **0''.05**, taking the peak flux density on the published image, frequency corrected from 8.4 GHz to 1.6 GHz using the integrated radio spectral index quoted by CHYT. The resulting value is a strict **upper** limit, unless the nuclear spectral index is steeper than that of the entire galaxy, a most unlikely circumstance given the nuclear concentration of energy generation and concomitant particle acceleration. If the nuclear spectral index is flatter than the integrated emission, or if there are significant contributions to the peak flux density from extended features these values will be reduced. In some cases, the presence of significant extended emission in the published image and the fitted component size in Table 2 of CHYT prompted the use of significantly lower values on the basis that extended emission contributes the major part of the peak flux density. These estimated maximum flux densities, $S_{\text{vlbi}}^{\text{max}}$, are listed in Column 13 of Table 1.

We compared our derived maximum possible compact 18cm flux densities to the detection thresholds on the most sensitive VLBI baselines accessible to each source, and included in our sample only those for which the flux density exceeded the detection threshold by at least a factor of two. The resulting source list comprises 31 sources which are listed in Table 2. The VLBI-detectability criterion is primarily a radio flux density limit because detectable compact structure could not be excluded for any object purely on the basis of resolved appearance on the CHYT image. It is almost certainly valid to consider systems excluded from the sample as non-detections at the detection threshold used to determine sample membership for that galaxy.

3. OBSERVATIONS

3.1. 18cm VLBI Survey Observations

The VLBI observations were performed on 1991 September 29, under the auspices of the U.S and European VLBI networks, project code GL5. In addition to the most sensitive antennas available, namely Effelsberg (Germany), phased VLA (New Mexico), Greenbank (West Virginia) and Arecibo (Puerto Rico), we used the south-western U.S. VLBA antennas Pietown and Los Alamos (New Mexico), Kitt Peak (Arizona), and Fort Davis (Texas), together with the Westerbork tied array (Netherlands) and the Jodrell Bank MkIA telescope (U. K.) to provide a number of relatively short baselines. Data reduction has been described previously in Paper I.

In all, 21 sources exhibited significant correlated flux density on one or more baselines, with detection thresholds as low as 1mJy on the most sensitive baselines. Visibility plots — correlated flux density versus baseline length --- were constructed for all sources detected on any baselines(s). The results of our global VLBI survey are graphically illustrated in Figure 1, which shows these visibility plots for the 16 sources with detections on multiple baselines and with implied source brightness temperature in excess of 10^6 K. Plotted for reference on each source plot is the expected behaviour for a single, gaussian source with $T_b = 10^5$ K (solid line), 10^6 K (dashed line), and 10^7 K (dotted line) at the scale of the appropriate baseline. A single detection along one of the plotted

curves sets a lower limit to the source brightness temperature under the assumption that the source is a circularly symmetric gaussian. Such a gaussian source would have an angular size, FWHM = 0.5 times the fringe spacing for the appropriate baseline and a flux density 2.5 times the observed value at that baseline. $T_b = 10^5 K$ is the expected maximum brightness temperature assuming a thermal (HII) bremsstrahlung source with $T_e \approx 10^4 K$ contributing 10% of the radio emission with 90% coming from supernova produced synchrotrons plasma (Condon and Yin 1990):

$$T_b \leq T_e \left[1 + 10 \left(\frac{\nu}{1 GHz} \right)^{0.1-\alpha} \right] \leq 10^5 K, \quad (1)$$

The solid line thus represents a fiducial for sources which merit further scrutiny as possible AGN cores.

The results of the VLBI experiment are summarized in Table 2, which is an updated version of data presented in Paper I. Columns (1) and (2) repeat the source name and 1.49GHz flux density as given in Table 1. Column (3) gives the 1.49GHz radio power and column (4) the infrared-to-radio ratio, “ q ” (Condon, Anderson and Helou 1991). Note that the data in columns (2)–(4) refer to source properties *integrated over the entire system*. Columns (5)–(7) give the VLBI data: columns (5) and (6) list the maximum correlated flux density and power at 18cm on baselines of projected $length \geq 10^6 \lambda$. Column (7) provides an estimate of the source brightness temperature, determined by modelling the emission as a circular gaussian component of angular size approximately 0.5 times the fringe spacing, and flux density 2.5 times the correlated flux density. This is the minimum brightness temperature for a gaussian component fitting the measurement; in general we cannot rule out regions with T_b significantly higher than quoted. For a few sources the visibility functions are adequately fit by a single gaussian component, and we quote the T_b corresponding to this component. For single baseline detections we also quote the T_b for a gaussian component with the appropriate correlated flux density on the baseline detected. For the current data, meaningful estimates of T_b above about $10^7 K$ cannot be made, and in case-s of substantial correlated flux density on very long baseline-s we have tabulated $T_b \gg 10^7 K$ (note that this does not imply pointlike, unresolved structure).

The median VLBI core power on baselines longer than $10^6 \lambda$ is $\log P_{\text{vlbi}}(\text{median}) = 22.06 (WHz^{-1})$ for detected sources, with a median ratio of core to total **1.6GHz** radio power of 12%. Figure 2 shows the histograms of the VLBI-core power and core fraction *limits* for detected and undetected sources. The two histograms are quite comparable, with median values $\log P_{\text{vlbi}} \lesssim 21.8 (WHz^{-1})$ and core fraction $\lesssim 6\%$, respectively. We caution that the flux density limits for undetected sources were typically determined on longer baselines than the maximum core flux density measurements for the detected sources. Nonetheless, our results are clearly consistent with the presence of compact high- T_b emission in all of our sample galaxies and in the majority of the CHYT complete sample, at a power level of $\log P_{\text{vlbi}} \gtrsim 22.5 (WHz^{-1})$ (which falls below the typical detection threshold).

All 17 sources with measured S_{vlbi} values listed in Table 2 have detectable compact emission substantially (i.e. more than a factor of 10) in excess of the Starburst limit of $10^5 K$ given by Equation (1). Three additional sources showed emission with $5.0 \lesssim \log T_b \lesssim 5.4$, only marginally above this limit. As anticipated from the CHYT images, most sources showed evidence for considerable emission on the shortest baselines (scales of 0.05 arcsec and greater).

By looking for **departures** from monotonically declining or flat curves on these plots, and combining this information with closure phase data, Paper I classified the structure as simple or complex, where “complex” can generally be taken to imply a lack of circular symmetry, and the strong possibility of multiple peaks in the brightness distribution at the resolution of the observations. Such classification was not possible for all detected sources, due to the paucity of data. This classification is indicated in column 7 of Table 2. It should be emphasized that future, more extensive observations may detect complex structure for sources classified here as “simple”, and this classification should not be taken as proof of pointlike structure. A designation of “complex” in Table 2, however, precludes the possibility that the detected emission originates in a single pointlike source.

3.2. High Resolution VLA Observations

In order to probe the structure of the intermediate-scale radio emission, and determine its relationship, if any, to the **VLBI-scale** emission, we used the VLA at its maximum angular resolution on 16 of the sources which showed **18cm VLBI-scale** emission above a brightness temperature of 10^5 K. Three sources were omitted because they could not be conveniently observed in the scheduled time allocation, and Mrk 231 was omitted on the basis that the bulk of the emission originates in an unresolved core component.

The observations were conducted during a 12-hour period on 1994 March 26 and March 27, in the A-array of the VLA. Data were taken for each of the 16 target sources at both K-band (**22GHz**) and U-band (**15 GHz**). An aggressive strategy for phase calibration, using nearby reference sources for each target, was employed. This involved rapid switching between calibrator and target, with 90 seconds on the calibrator and 150 seconds on the target, inclusive of slewing time, for a total cycle time of 4 minutes. The sources were divided into two groups for scheduling, designated strong and weak on the basis of the anticipated correlated flux density, estimated using the CHYT images and our 18cm VLBI data, with assumed spectral indices. The weak sources were allocated” roughly 21 minutes of on-source integration time at K-band, and 13 minutes at U-band, compared to 8 minutes and 4 minutes respectively for the strong sources. The anticipated final map **r.m.s.** noise levels ranged from 0.15 mJy to 0.5 **mJ** y per beam.

The weather was poor during the observations, with moderate cloud cover and intermittent snow showers. Phase stability was poor during the first hour or so, and snow accumulation in the dishes effectively destroyed the final 90 minutes of the run. The data for two sources, Arp 220 and NGC 6286, were useless. The data were reduced using the NRAO AIPS software package at Haystack Observatory. Several phase calibration methods and many diagnostics were employed to maximize and measure the quality of the final phase calibration; a simple two-point interpolation scheme using adjacent calibrator scans was found to be optimal. In a few cases, reliable self-calibration of the target source was possible, allowing us to accurately assess the quality of the external phase calibration in those cases. For most of the source-s, the loss of peak intensity due

to phase errors is thought to be less than 10% at U-band and 20% at K-band, with higher values possible toward the beginning and end of the run. The majority of the images presented here are noise-limited, and cases in which there is doubt about the image fidelity are discussed individually. The overall flux density scale was fixed using observations of 3C286 during the run, in the standard manner. The images were produced using the CLEAN algorithm. In cases where self-calibration was possible, a single cycle of phase-only self-calibration with a short solution interval was employed.

It is evident from these observations, as with the VLBI visibility data, that structure typically exists on a range of size scales. However, due to generally low image SNRs, it is impossible to represent the detected structure on the highest spatial scales simultaneously with the lowest surface brightness extended emission. We have therefore chosen to present in Figure 3 the data for each source using an array of four images of decreasing angular resolution, but increasing sensitivity: 22GHz uniform weighting, 22GHz natural weighting, 15GHz Uniform weighting and 15GHz natural or tapered. For each source we also present the VLA restoring beam and the FWHM ellipse of the deconvolved gaussian fitted by CHYT for that source to indicate graphically the extent of the substructure detected in our higher-resolution observations.

3.3. Optical Spectrophotometry

New optical observations for several of our sample galaxies which have no previously published quantitative optical spectrophotometry were obtained in 1992 and 1993 using the Kast Double CCD Spectrograph on the 3-m Shane Telescope of UC’s Lick Observatory. The optical data were reduced using the NOAO IRAF reduction package at the Infrared Processing and Analysis Center (IPAC). The spectra were extracted using IRAF’s optimal extraction procedure with windows typically 7-10” perpendicular to the dispersion. Sky was taken well away from the galaxy nucleus — typically further than 15”- but in most cases may still contain some residual emission. The wavelength calibration was initially performed using calibration lamp observations from the beginning and/or end of the night, but the individual spectra were recalibrated using the extracted night sky spectrum for each object, resulting in a wavelength accuracy of approximately 0.5Å. A variety of IRAF

procedures were used to estimate line fluxes; blended features were separated using IRAF’s gaussian spectral fitting procedure. Except where noted, uncertainties in the relative line fluxes are estimated to be about 10%.

Veilleux *et al.* (1995) have recently published an extensive spectrophotometric survey of luminous and warm IRAS galaxies, which contains many of the systems in our sample. Along with previously published data from Armus, Heckman and Miley (1989), we now have high-quality quantitative measures for all but one system in the LFIRG Sample.

In Table 3 we list the red ($\lambda \approx 4800\text{--}7200$) spectrophotometric data for our sample galaxies in terms of reddening corrected ratios of the principal excitation-sensitive features: $\frac{[OIII](\lambda 5007)}{H\beta}$, $\frac{[NII](\lambda 6583)}{H\alpha}$, $\frac{[SII](\lambda 6717+\lambda 6730)}{H\alpha}$, and $\frac{[OI](\lambda 6300)}{H\alpha}$. The line ratios have been used to calculate optical spectroscopic excitation values following the scheme first suggested by Baldwin, Phillips, and Terlevich (1981). In Figure 4, we plot the excitation of the sample members from the $\frac{[OIII]}{H\beta}$ vs $\frac{[NII]}{H\alpha}$ relation, where each galaxy is plotted with a symbol indicating T_b . The HII/AGN boundary follows the version of this scheme of Veilleux and Osterbrock (1987). This diagram is the basis for the optical spectral classification listed in Table 3. Although the Spectral Types would appear to be evenly mixed between HII and AGN classification, we note, as originally emphasized by Sanders *et al.* (1988), that the HII Galaxies all lie very close to the HII/AGN boundary, with much higher excitation than typical Galactic HII regions and well above the locus of HII models. On the other-hand the majority of AGN systems are, in fact, LINERS, (Veilleux *et al.* 1995) rather than exhibiting classical Seyfert/QSO excitation.

We are, unfortunately, unable to draw firm conclusions based on the optical spectra of our sample. The systems are high-excitation for star-forming systems, but low-excitation for AGN. Of particular note is the fact that the emission line spectrum yields few, if any, clues to the existence of VLBI-scale radio emission. In Figure 4 it is apparent that the distributions of the high T_b , intermediate T_b , and undetected sources are not significantly different. Given the amount of obscuring material estimated to be present in the LFIRG nuclei, it is hardly surprising that physical relationships are also obscured. Infrared spectrophotometric observations (e.g. Spinoglio

& Malkan 1992, Voit 1992) may potentially provide a more conclusive **discriminant**, as, for example in the **case** of recent ISO observations of Arp 220 (**Sturm *et al.* 1996**) which show no high-excitation mid-infrared features, suggesting a thermal ionizing radiation field in that object.

4. DISCUSSION

4.1. Statistical Analysis

We have used Survival Analysis (Isobe, Feigelson and Nelson 1986) statistical techniques to compare the compact VLBI flux densities, S_{vlbi} , VLBI powers, P_{vlbi} , and 1.5 GHz core-fractions, $\frac{P_{\text{vlbi}}}{P_{\text{total}}}$, with the other known radio, infrared and optical characteristics of our sample galaxies listed in Tables 1–3. We restrict this analysis to the 31 galaxies in our VLBI experiment so that for most tests there are 17 detections and 14 limits to VLBI power and core-fraction. The presence of radio upper limits dictates the use of Survival Analysis and we have employed two correlation tests: Cox’s Hazard Test (parametric, assuming a Gaussian error distribution) and the Generalized Kendall’s Tau (BHK, nonparametric) Test, with equivalent results. Table 4 lists the results of the **Cox-Hazard** correlation test, which provides the familiar χ^2 statistic as estimator of the correlation strength. Potential correlations between VLBI properties and several other observable were examined. These include: far-infrared (FIR) flux density and luminosity, (%) color, $\left(\frac{60\mu}{100\mu}\right)$ color, $60\mu\text{m}$ spectral shape, $C_{60\mu}$, FIR to radio ratio, q , radio spectral index, $\alpha_{1.49}^{8.44}$, H_2 gas mass, inferred from CO observations, and FIR to M_{H_2} ratio (sometimes called the “star-formation efficiency”). None of the above correlations are sufficiently strong to provide a compelling case for a physical relationship. We examine briefly those correlations with probability, $P \leq 0.10$, smaller than 10% for a chance occurrence. Seventeen basic relationships are tested; we would thus expect there to be a couple of chance correlations among unrelated parameters and there are five: (1) infrared luminosity with VLBI power, (2) total 1.49 GHz radio power with VLBI power, (3) molecular gas mass (CO luminosity) with VLBI power, (4) radio spectral index with VLBI power, and (5) with VLBI fraction,

In a previous paper (LSL95) we examined the relationship (1) between far-infrared luminosity and VLBI core power. While this relationship is not highly significant ($P = 870$), LSL95 showed that there is a common relationship between luminosity and VLBI power for **LFIRGs** and radio-quiet quasars, suggesting a possible physical relationship. Unfortunately, this relationship is not a discriminator between AGN and Starburst models. If the compact, high- T_b emission in **LFIRGs** comes from Starburst generated radio supernovae, then the supernova rate, hence the compact radio emission, should scale directly with the star-formation rate, as does the infrared luminosity. The second observed correlation, between total radio power and VLBI power ($P = 1\%$), is also present, though at lower significance ($P = 9\%$), in the total **flux** vs. VLBI flux relationship, and suggests that there is a physical relationship between the mechanisms producing the compact and extended radio power. The presence of the third correlation, between the mass of molecular gas, inferred from CO observations, and VLBI power ($P = 5\%$), is to be expected if Starburst generated RSN produce the **VLBI-scale** emission, or, in hybrid Starburst/AGN models, if Starburst-related winds or supernovae provide the fuel for accretion onto a compact object in the AGN core (Norman & Scoville 1988, Perry & Dyson 1985).

The radio spectral index may be expected to have a value, $\alpha_{1.49}^{8.44} \approx 0.7$, appropriate for **optically-thin** synchrotrons emission, which may then be “flattened” by free-free absorption or by the presence of multiple, compact, self-absorbed synchrotrons components. CHYT interpreted these galaxies as **ultracompact** starbursts with thermal dust emission at $T \approx 60 - 80\text{K}$ and densities so large as to be optically thick to free-free absorption at 1.6GHz and to dust extinction at $25\mu\text{m}$. (For this reason we have avoided **mid-IR** quantities, $\lambda \leq 20\mu\text{m}$, where $\tau_{\text{dust}} \gtrsim 1$ and where there are also many censored data points.) In either case, the spectral index may be taken as a measure of compactness and the correlations in VLBI power and VLBI fraction with spectral index suggest that compactness on VLA scales is related to the presence of VLBI emission.

With the exception of Mrk 231 there is no evidence for self-absorbed synchrotrons components in these sources, but there is certainly ionized gas capable of producing free-free absorption. We have made optical depth corrections to the appropriate radio quantities following CHYT, by assuming

a uniform intrinsic spectral index, $\alpha_0 = 0.70$, between 1.49 and 8.44 GHz. Because the free-free optical depth, $\tau_{ff} \propto \lambda^2$, there will not be significant optical depth at 8.44GHz. In this case:

$$\tau_{ff} \approx 2.3(\alpha_0 - \alpha_{1.49}^{8.44}). \quad (2)$$

The inferred optical depths are $0 \leq \tau_{ff} \leq 1.36$, excluding Mrk 231, a “consensus monster,” with a presumed inherently flat spectrum. This reduces the mean **FIR-to-radio** ratio from $\langle q \rangle = 2.48$, to $\langle q' \rangle = 2.39$ (again excluding Mrk 231), closer to the well defined mean value, $q = 2.34$, observed for the *BGS* as a whole. If the inferred *integrated* free-free optical depths are correct, then the **1.6GHz** VLBI power, which likely originates in the innermost obscured regions of the source, must probably be corrected for even larger optical depths. Applying the optical-depth correction inferred above does not significantly alter the median core power, because most of the lower luminosity sources have steep spectra and low inferred optical depth, but it raises the upper envelope of VLBI power to in excess of $\log P_{vlbi} = 23$ (Jy/Hz). The corrected quantities, q' , P'_{vlbi} , and $P'_{1.49}$, are listed in Table 5. The correlation tests were also performed with the corrected radio parameters and the results are listed in Table 4, as well. In many cases there is a small improvement in the significance of correlations with P'_{vlbi} . (Note that the core-fraction is not altered by this correction.) For example, the probability of chance occurrence decreases from 8% to 5% for L_{FIR} vs P'_{vlbi} . Also, there is now an apparently significant (inverse) correlation between corrected radio-infrared parameter, q' , and P'_{vlbi} . If AGN contribute to the flux density at a measurable level, this may suggest that AGN activity contributes a greater share of the radio than the infrared. This is at variance with the results of LSL95 which indicate that radio-quiet quasars have a *higher* ratio of L_{bol} to $P_{1.49}$ than do LFIRGs.

We have, for comparison, tested relationships between infrared luminosity and the other physical characteristics listed in Table 1. A number of correlations, found previously for the *BGS* as a whole, are shown to **hold** for the LFIRG sample: molecular gas mass and infrared luminosity, FIR color and infrared luminosity, and the well-known radio-infrared correlation. For this sample we also find significant correlations between L_{FIR} and spectral index and FIR-radio ratio, q .

The correlation between M_{H_2} and L_{FIR} has been well studied (Sanders, **Scoville** and Soifer 1991, Solomon *et al.* 1992, 1997) and strongly suggests that star-formation is occurring in these gas-rich systems. However, recent evidence suggests that the geometry of the molecular gas in LFIRGs is disk-like, rather than GMC structures (**Scoville**, Yun & Bryant 1997, Bryant & **Scoville** 1996), and one might expect that the relationship between the star-formation rate and gas mass may accordingly be different. Indeed, the best fit regression lines to the 35 galaxies with $H_2(CO)$ measures finds a flatter relationship with a luminosity intercept at about $L = 1.5 \times 10^{11} L_{\odot}$, suggesting a lower star-formation rate per unit gas mass plus a possible additional component to the luminosity. Similar results have been obtained by Solomon *et al.* (1997) and Sanders, **Scoville** and Soifer (1991) with differing interpretations.

Relationships between infrared colors and luminosity have been discussed previously and used to select for AGN candidates in the IRAS databases (Low *et al.* 1988, 1989). Very simple models for infrared emission from hot dust surrounding either AGN or Starbursts can plausibly explain such a relationship. The LFIRGs are compact as a class, with radio emission typically confined to a region, $\theta \lesssim 0''.25$ (CHYT), thus the correlation between infrared luminosity and spectral index may likely be a continuation of the trend toward compactness with increasing luminosity. Given there is a fairly significant correlation between $\alpha_{1.49}^{8.44}$ and L_{FIR} and a weak correlation between L_{FIR} and P_{VLBI} it is not surprising that there is also a weak correlation between $\alpha_{1.49}^{8.44}$ and P_{VLBI} . The only highly significant ($P < 1\%$) correlation among these characteristics is the radio-infrared correlation. As noted by CHYT, correction for free-free optical depth not only reduces the infrared-radio parameter, q , to a value closer to the mean for starburst galaxies, but strengthens the correlation (Mrk 231 is included in the correlation test, but not corrected for free-free extinction).

Taken as a whole, these statistical relationships strongly suggest that there is a continuity between the LFIRGs and lower luminosity Starbursts in physical characteristics. Furthermore, the molecular gas emission, infrared luminosity and radio power on VLA–VLBI scales appear to be physically related. Active star-formation is certainly occurring in the majority of these LFIRGs and our statistical analysis is consistent with a Starburst origin for the radio, millimeter, and infrared

emission. This analysis does also admit for the possibility of a hybrid or dual nature (e.g. Starburst and AGN) for the **LFIRGs**. Although the relationships between VLBI and other characteristics are suggestive, they do not provide a statistical framework for interpretation of the VLBI emission in terms of either Starbursts or AGN, nor do the correlations suggest an evolutionary path from one to the other.

4.2. Starburst Models

As described above, LSL95 showed that it is plausible that the **LFIRGs** are powered by AGN with radio core properties comparable to those of radio-quiet **QSOs**. Now we ask the complementary question: is it plausible that the **LFIRGs** are powered by Starbursts? We examine simple Starburst models for the LFIRGs in order to examine whether such models lead us to fundamental physical difficulties and to estimate the star-formation rate, supernova frequency and other parameters which may be used for interpretation of our results.

For a power-law Initial Mass Function function, $\psi(m) \propto m^{-\gamma}$ (e.g. $\gamma = -2.5$, $m > 1M_{\odot}$ following Miller and Scalo, 1979) one may create heuristic scaling-law models for observable features of a Starburst in terms of the star-formation rate, \dot{m} , and m_l and m_u , the lower-mass cutoff and upper-mass cutoff for star formation. Here we follow Scoville and Soifer (1991) who employ a modified **Miller-Scalo** IMF to derive the **bolometric** (in this case far-infrared) luminosity for a **constant** star-formation rate Starburst:

$$L_{FIR} = 1.2 \times 10^{10} L_{\odot} \left(\frac{m_l}{1M_{\odot}} \right)^{\alpha} \left(\frac{m_u}{45M_{\odot}} \right)^{0.37} \left(\frac{\Delta t_{*b}}{10^8 yr} \right)^{0.67} \dot{m} (M_{\odot} yr^{-1}) \quad (3)$$

where Δt_{*b} is the starburst lifetime, and $\alpha = 0.23$ for $m_l < 1M_{\odot}$. Unfortunately the parameters m_l, m_u , and Δt_{*b} are poorly constrained even for *bona-fide* Starbursts. There is strong evidence that $10^7 yr \leq \Delta t_{*b} \leq 10^9 yr$; for interaction triggered Starbursts one would expect the duration to be of order of the dynamical time, $\Delta t_d \sim 10^8 yr$. A number of considerations suggest that the IMF is truncated at lower initial mass and does not extend below about $1M_{\odot}$ (Scalo 1986), but the

actual mass at which the IMF stops is controversial and may vary from system to system; m_u which determines the heating rate and the flux of ionizing photons is virtually unknown from independent arguments. For the remaining discussion we will adopt $m_l = 1M_\odot$, $m_u = 45M_\odot$ and $\Delta t_{*b} = 10^8 yr$. If we consider a “typical LFIRG” with $\log L_{FIR} = 11.5$, the implied star-formation rate, $SFR = m = 27M_\odot yr^{-1}$.

The Lyman continuum photon flux is given by:

$$N(\nu > \nu_0) = 9.85 \times 10^{52} s^{-1} \left(\frac{m_l}{1M_\odot} \right)^\alpha \left(\frac{m_u}{45M_\odot} \right)^\beta \dot{m} (M_\odot yr^{-1}) \quad (4)$$

where $\beta = 2.00$ for $m_u < 45M_\odot$ and $\beta = 1.35$ for $m_u > 45M_\odot$. From this we may calculate the radio power from thermal *bremsstrahlung*:

$$P_\nu(f - f) = 2.6 \times 10^{21} W Hz^{-1} g_{ff} \frac{e^{-h\nu/kT}}{T^{1/2}} \left(\frac{m_l}{1M_\odot} \right)^\alpha \left(\frac{m_u}{45M_\odot} \right)^\beta \dot{m} (M_\odot yr^{-1}) \quad (5)$$

which for $T = 10,000K$ at a frequency $\nu = 1.5GHz$ reduces to:

$$P_{1.5GHz}(f - f) = 1.58 \times 10^{-33} W Hz^{-1} N(\nu > \nu_0) \quad (6)$$

Condon and Yin (1990) suggest that there is a fairly universal **nonthermal** to thermal ratio of radio emission:

$$\left\langle \frac{P_{nt}}{P_{ff}} \right\rangle \approx 10 \left(\frac{\nu}{1.5GHz} \right)^{0.1-\alpha} \quad (7)$$

where the **nonthermal** spectral index $\alpha \approx 0.7$. We then estimate a total 1.5GHz power, $P \approx 3.2 \times 10^{22} W Hz^{-1}$.

However, the radio-infrared ratio, q , defined in terms of L_{FIR} and $P_{1.5GHz}$ suggests a different nonthermal/thermal ratio:

$$q = \log \left\{ \frac{[L_{FIR} * L_\odot / 3.75 \times 10^{12} LO]}{P_{1.5GHz}} \right\} \quad (8)$$

such that,

$$q \approx 3.76 - \log \left[\left\langle \frac{P_{nt}}{P_{ff}} \right\rangle + 1 \right] + (0.37 - \beta) \log \left[\frac{m_u}{45M_\odot} \right] + 0.67 \log \left[\frac{\Delta t_{*b}}{10^8 yr} \right] \quad (9)$$

For our model, we calculate $q \approx 2.81$, nearly a factor of 3 higher than the canonical value ($q \approx 2.34$ for the BGS (Condon, Anderson and Helou 1991). Adopting $q = 2.34$ then requires a nonthermal to thermal ratio:

$$\left\langle \frac{P_{nt}}{P_{ff}} \right\rangle \approx 30 \left(\frac{\nu}{1 \text{GHz}} \right)^{0.1-\alpha} \quad (10)$$

which we adopt for the purposes of consistency.

Of particular interest for understanding the origin of **LFIR** radio emission is the supernova rate. For a population with minimum initial mass for supernova detonation, m_{sn} , the supernova rate:

$$\nu_{sn} = \int_{m_{sn}}^{m_u} \psi(m) dm \approx \frac{\dot{m}}{3} \cdot \frac{(m_{sn}^{-1.5} - m_u^{-1.5})}{(m_l^{0.5} - m_u^{0.5})} \quad (11)$$

for $m_l \geq 1.0 M_\odot$. For $m_{sn} = 8 M_\odot$ our typical LFIR Galaxy, with fog $L_{FIR} = 11.5$, would have a supernova rate, $\nu_{sn} \approx 0.4 \text{ yr}^{-1}$. Provided that the **nonthermal** radio emission is produced by **Starburst-related** supernovae and remnants, there should exist a direct relationship between P_{nt} , and ν_{sn} . Condon and Yin (1990) deduce a relation from the Galactic ratio of **nonthermal** luminosity to production of radio-emitting supernova remnants; scaling their result to **1.5GHz** yields:

$$\nu_{sn} (\text{yr}^{-1}) \approx \frac{P_{nt}}{10^{23} \text{W Hz-l}} \quad (12)$$

which is within a factor of two agreement with the above. The supernova rates from our model predictions are not very sensitive to the input assumptions because the supernovae come principally from the middle of the IMF.

Table 5 lists the Starburst model parameters for each of our sample galaxies. These were calculated using the above prescription with a star-formation rate that reproduces the observed infrared luminosity, L_{FIR} , according to equation (3). Also listed are results for two other **scaling-law** models which adopt differing upper and lower mass limits to the IMF: a “high mass” model with $m_l = m_{sn} = 8 M_\odot$, and an extended IMF model with $m_l = 0.1 M_\odot$ and $m_u = 60 M_\odot$. Note that the star-formation rate varies by nearly a factor of 5 among these prescriptions, but the supernova frequency is much less sensitive, varying by less than 50%.

Such scaling-law models have been superseded by more sophisticated calculations which use stellar population synthesis to calculate detailed Starburst characteristics **as** a function of time. We have employed the models of Leitherer and Heckman (1995) to make comparable calculations for our LFIRG sample. The results from applying their fundamental, constant SFR (continuous star formation) model ($\gamma = -2.35$; $m_l = 1M_\odot$; $m_u = 100A_4$; $Z = 1 - 2Z_\odot$) are also shown in Table 5. These results are quite comparable to the global characteristics of the simple parameterized models with similar input. While the more sophisticated models are very powerful in modelling the detailed characteristics of individual systems with extensive observational data sets, the simple calculations appear adequate to provide comparative results for our sample, especially considering the uncertainties in the input parameters.

The Starburst models are viable, in the sense that they match the gross observational characteristics of our sample galaxies with parameters that are within range of current expectation. For example, $t_{*b} \approx 10^8 \text{ yr}$, equal to the dynamical timescale for galaxy interaction/merger, is a modest fraction of the total Starburst lifetime, estimated by the time necessary to exhaust the available store of molecular gas at the inferred star-formation rate. Similarly, the upper end of the main sequence produces the appropriate flux of ionizing photons to produce the observed dereddened $H\alpha$ luminosities. This apparent agreement may be fortuitous, however, since the $H\alpha$ luminosities do not allow for internal absorption in a dusty ionized medium, nor for absorption of ionizing photons on dust grains. This consistency is relatively minor comfort, given the number of free parameters and our scant knowledge about the IMF. The principal result here is that the LFIRGs may be modelled with similar plausibility under the Starburst paradigm as with the AGN (LSL95). Similar conclusions have been reached by other workers (c. f. Scoville & Soifer 1991, Leitherer & Heckman 1995). In individual cases, more detailed observations have placed more stringent constraints on the models. For example, in Arp 220, an upper limit on the 2.6mm continuum (Scoville *et al.* 1991) constrains the free-free flux density and thus the ionizing photon flux, $N(\nu > \nu_0)$, which in turn places a limit, $m_u \lesssim 30M_\odot$, and dynamical mass estimates appear to constrain the lower mass limit, $m_l \gtrsim 5M_\odot$ (Scoville *et al.* 1997).

Accepting that Starburst models are generally plausible, a fundamental question remains: Under Starburst models, what is the origin of the compact VLBI emission and its relationship to the Starburst event? Might these be luminous Radio Supernovae (singly or in clumps)? Or a compact massive object fundamentally unrelated to the Starburst and the galaxy energetic? Under the AGN model, what is the origin of the **VLA-scale** radio emission and why does it produce the same radio-infrared ratio, q , as Starbursts? Is the intermediate scale radio emission the product of a Starburst which is the mechanism for fueling the central engine?

4.3. The Origin of the VLBI Emission: RSN vs AGN

Our prejudice at the outset of this research was that compact, high T_b radio emission is a unique indicator of an AGN core. However, it has become clear in recent years that there exists a distinct class of radio supernovae which exhibit very high radio power (Wilkinson&de Bruyn 1990) and which may, in the extreme, compete as candidates for the compact VLBI emission detected in this study. Given the high expected supernova rate for luminous Starbursts from Table 5 above, $0.1 \lesssim \nu_{sn} \lesssim 2$, our sample galaxies will have frequent supernovae and it is plausible to suspect that such extreme Starbursts will give rise to luminous RSN *if their dominant energy source is from star-formation*. The best studied member of this class is SN1986J in NGC 891 (Weiler *et al.* 1990) which exhibited a maximum radio power, $\log P_{1.5\text{GHz}}(1986J) = 21.15$.³ Even more extreme, a compact variable radio source in the Starburst galaxy Markarian 297 — Mrk 297A (LLS92, Yin and Heeschen 1991) — has been interpreted as the most luminous RSN observed to date, with a 1.5GHz power at maximum, $\log P_{1.5\text{GHz}}(max) = 21.5 (W Hz^{-1})$.

Only one of the VLBI sources in Table 2 has a VLBI power, $\log P_{vlbi} < 21.5 (W Hz^{-1})$, the largest

³We adopt a distance $d = 9.5 Mpc$ to NGC 891. NGC 891 is a member of the NGC 1023 Group, which includes NGC 925. An HST/cepheid distance to NGC 925, $d = 9.3 \pm 0.7 Mpc$ has recently been measured by Silberman *et al.* (1996). An independent measurement for NGC 891 based on planetary nebulae, $d = 9.9 \pm 0.8 Mpc$, has been made by Ciardullo *et al.* (1991).

value previously attributed to a luminous **RSN at maximum light**. Seven sources are within a factor of three of this value, however, and we must ask if the luminous RSN may plausibly exhibit such high radio power. Unfortunately, **phenomenological** models which can provide an excellent fit to RSN light curves do not constrain the energy budget because they allow the particle/field energy to scale as an arbitrary fraction of SN shock energy (Chevalier 1982). Physical models of shock acceleration of synchrotrons electrons in dense nuclear environments which can provide realistic estimates of RSN luminosities have not yet been developed (*c.f.* Jones and Kang 1993). We note however that a standard synchrotrons model for Mrk 297A implies an equipartition particle/field energy $U_{int} \approx 4 \times 10^{49} \text{erg}$ (LLS92), which is an uncomfortable **4%** of the available kinetic energy budget, 10^{51}erg , allocated to Type II supernovae. Unless a physically new, more energetic class of SN explosion is postulated, we believe that it is reasonable to consider $\log P_{vlbi} = 21.5$ as the maximum value for a single supernova. In this context, it is worth noting that **70%** of SN will have progenitor masses within a factor of two of the lower mass limit for SN detonation (*i.e.* between $8\text{-}16M_{\odot}$). Appealing to supermassive stars as a way to produce a new class of very luminous supernova would appear to be unable to explain the frequency of compact **VLBI-scale** emission.

Finally, the majority of sources with compact, **high- T_b** emission show complex structure which could not be replicated by a single RSN. We conclude that luminous RSN cannot, as isolated events, produce the observed VLBI emission. We address the possibility that multiple RSN may produce the compact, high T_b emission in Section 4.3.2, below.

4.3.1. *AGN Source Structure*

Another approach to the origin of the compact radio emission is to compare the source structure, inferred principally from the observed visibility curves, with structure expected from AGN or Starburst sources. The LFIRG visibility functions displayed in Figure 1 show a variety of characteristics. The slopes of the visibility curves show a large range, frequently without discernible structure indicating a preferred spatial scale. In some cases there is evidence for separate large and small scale structures, with high flux densities on short baselines and a constant low flux density

level on intermediate and long baselines. Occasionally, hints exist of complicated structure, in the form of extreme departures from a monotonic decline with baseline length. Common to all these curves, however, is the tendency for structure to exist on a variety of scales, with no apparent preferred spatial scale. This inference is borne out by the VLA imaging study. Despite the large difference in observing frequencies, which hampers quantitative comparisons, it is clear that sub-structure is ubiquitous in these objects on the $0''.1$ scale as well as on the smaller scales accessible to the VLBI survey. This supports a picture in which material is clumped on all scales between a few parsecs and a few hundred parsecs.

For comparison with the structures observed in the LFIRGs there is a wealth of VLBI data for AGN available in the literature. The most comprehensive data set is the Caltech-Jodrell Bank VLBI Survey with 18cm global VLBI observations of in excess of 100 sources (Polatidis *et al.* 1995, Thakkar *et al.* 1995) with supporting VLBI/MERLIN observations at 6cm and VLA observations at 21cm (Xu *et al.* 1995). Although the data are not yet fully interpreted, and visibility functions are not presented for direct comparison with our results, the structural models (maps) presented show a large variety of structures within known AGN. These range from sources with unresolved cores, with or without jets, through multiple components, to fairly diffuse structures. In many cases structures are present on a variety of spatial scales comparable to the scales of interest in our study. Without doubt our observed VLBI visibility functions and VLA images may be accommodated within the varied ensemble of structures associated with AGN.

4.3.2. *Starburst Models: Synthetic Visibility Functions for RSN*

While it appears impossible for a single powerful Type 11 RSN to provide the necessary VLBI power, there is no conclusive evidence that the compact milliarcsecond power is provided by a single source. Table 5 indicates a typical supernova rate of $1/2 \text{ yr}^{-1}$. If all of these supernovae are radio-luminous with a decay time of order 10 years, typically 5-20 luminous RSN could, in principle, contribute to compact, unresolved ($\theta \lesssim 0''.001$) structure and thus to the visibility function at the longest baselines. We have modelled the visibility functions for compact Starbursts dominated (in

the radio) by radio supernovae and attempted to fit these models to those members of our VLBI sample whose visibility functions are adequately determined.

We construct Monte-Carlo models which fill a spherical volume of diameter corresponding to the VLA radio source size with randomly distributed or clumped RSN which detonate at random intervals, then decay following observed RSN decay rates. LLSL92 discussed RSN in this context in some detail; the underlying theory, due principally to Chevalier (1982), has been applied to RSN by Weiler *et al.* (1986, 1990). The RSN light curve is interpreted as an optically thick, thermal supernova shell expanding into a dense ambient medium, presumed to be the supergiant progenitor’s stellar wind:

$$S_\nu \propto \nu^\alpha t^\beta e^{-\tau} \quad (13)$$

where α is the spectral index, $\alpha \approx -0.7$, t is the time since detonation, and τ is the optical depth. Because the rise in the light curve to maximum light is quite rapid as the optical depth decreases, we adopt

$$S_\nu = \frac{P_\nu(\max) t - t_0}{4\pi d^2 (3 \text{ yrs})}^\beta \quad (14)$$

where $P(\max)$ is the power at maximum light, which is taken to be 3 years after detonation at $t = t_0$ (Weiler *et al.* 1986). We employ two Type II RSN classes.:

1) Standard RSN: Typical radio supernovae have peak radio powers up to $P_{1.5\text{GHz}}(\max) \approx 2 \times 10^{20} \text{ W Hz}^{-1}$. They are generally well fit by the above model with $\langle \beta \rangle \approx -0.7$ (Weiler *et al.* 1986). We adopt $P_{1.5\text{GHz}}(\max) = 10^{20} \text{ W Hz}^{-1}$ and $\beta = -0.7$ for standard RSN.

2) Luminous RSN: We adopt SN1986J, $P_{1.5\text{GHz}}(\max) = 1.4 \times 10^{21} \text{ W Hz}^{-1}$, as a prototype of luminous RSN. In the case of luminous RSN the light curve is better fit with expansion into a thermal absorbing medium, presumed to be the ejected supernova shell, and nonthermal emitting medium, possibly at the shock interface with the ambient medium (Weiler *et al.* 1990). The shape of the rise to maximum, and the epoch of maximum light as a function of frequency, are affected by this model, but the light curve from maximum is still well fit by a power-law expression with

a steeper decline, $\beta = 1.2$. Mrk 297A has a similar “best fit” value of the decline rate, $\beta = 1.3$, although in both SN1986J and Mrk 297A the decline is irregular and not **always** monotonically decreasing post-maximum. For our **modelling** we will adopt $\beta = 1.3$ for luminous RSN, but let $P(\mathbf{max})$ scale in units of $P(1986J)$ to provide a best fit to the visibility functions.

We consider two spatial distributions of supernovae: 1) centrally concentrated using a spherically-symmetric, gaussian radial probability distribution with half-power points selected to correspond to the FWHM of the **deconvolved** 8.44GHz maps of CHYT, and 2) centrally concentrated as in (1), but clumped on parsec scales as might be the case, for example, if **Starbursts** form massive clusters of stars.

In the simple gaussian model the supernova are “detonated” randomly within the assumed spatial distribution and at random intervals which may be characterized by a supernova frequency, ν_{sn} , for comparison with the values obtained in our Starburst models. In a given model all RSN have a uniform power at maximum, $P(\mathbf{max})$. The supernovae then decay according to the above decay rates and expand with expansion velocity, $v_{sn} = 10,000 km s^{-1}$. The **modelled** RSN are effectively point sources because individual RSN tend to fade from view before they become significantly extended, particularly for the more distant sources and the more luminous RSN models, with the steeper decline in the light curve. The process is continued for 10^3 years to create what is effectively a constant distribution of bright supernovae, with a background population of fainter RSN and remnants that increase with t_{\bullet} . The supernovae are projected onto the sky plane, then the visibility function is sampled on the u-axis only, relying on circular symmetry and avoiding the complication of a full 2-D Fourier transform. The entire process is repeated 500 times and averaged to determine a mean visibility curve and rms variation as a function of baseline length. These **curves** are then compared with our survey observations. Since the size of the star-forming region is set by the **VLA** radio diameter measured by CHYT, only two parameters are varied in the “Standard RSN” model: S_{vbi} and ν_{sn} . For luminous RSN models the RSN power at 18cm is an additional fitted parameter.

In the clumped model, clumps of radio power, P_{cl} , are distributed according to the same gaussian **radial** probability distribution, with each clump subdivided into n_{sn} individual supernovae of power, $P_{sn} = \frac{P_{cl}}{n_{sn}}$. The n_{sn} individual **supernovae** are then distributed randomly **along** a segment of the x-axis of length corresponding to the clump size, d_{cl} , typically 1-10PC. The clump geometry is effectively a uniform cube with one axis along the line of sight. This will introduce power at the appropriate uv-distance in the visibility function, but will not reproduce appropriate substructure. Within the limitations of the observed visibility functions and the Monte-Carlo models, this is a minor **effect**. All the **supernovae** in a clump are **detonated** simultaneously and with **common** power. This may tend to induce greater variance between individual models than a more realistic staggered detonation model might yield, but, if the presence of clumping is to produce significant structure in the visibility function with reasonable RSN frequency, the supernova explosions in a given clump must occur over a **timescale** short with respect to the decay time of the RSN. In the limit, models with high spatial clumping but no temporal correlation are indistinguishable from the unclumped gaussian models in their radio emission. This provides an additional strong constraint on systems which are best fitted with clumped **RSN** models.

Figure 5 shows a suite of synthetic visibility functions for RSN models at a distance of **100Mpc**, with supernova rate $\nu_{sn} = 1yr^{-1}$ calculated to produce a VLBI flux density, $S_{vlbi} = 2mJy$ and total flux density 30mJy. Panel (a) shows the variation the visibility function with **RSN** luminosity at maximum, $P(max) = 0.25, 0.50, 1.0, 2.0, 4.0 \times P^{1986J}$ for a gaussian model. The model visibility **function** is characterized by a shoulder at short u-v distances, determined by the scale for which multiple RSN **fall** within a single interferometer lobe spacing. The visibility then falls off to a level which is determined by the maximum flux density per RSN and the RSN decay rate, which determines the number of individual RSN which contribute to the flux density. In most cases this is not a good match to the observed visibility functions which do not indicate any preferred spatial scale.

The clumping introduces power on intermediate u-v scales, which, depending upon the clump size, yields a more nearly featureless, power-law visibility function. Clumped models are shown

in panels (b) — (d). The fiducial model has eight supernovae per clump, $N_{sn}/cl = 8$, detonated simultaneously with $P_{cl} = 8 \times P^{1986J}$, hence $P_{sn} = 1.0 \times P^{1986J}$, in clumps with size, $d_{cl} = 4.0pc$. The effect of varying clump power, P_{cl} is shown in panel (b); in this case the number of RSN per clump is kept constant ($N_{sn}/cl = 8$), thus the individual RSN power also scales. Panel (c) shows the effect of varying the clump size. Finally, panel (d) shows the effect of the degree of clumping: clump luminosity is adjusted as number per clump was varied, maintaining constant RSN luminosity. Thus, we have a series of models with similar RSN which get progressively clumpier in their spatial distribution. The curves are labelled by N_{sn}/cl . Because the models represent the average of a large number of individually calculated visibility functions, fluctuations due to constructive and destructive interference of individual components are averaged out, resulting in models which are smoother than the observed visibility functions on the longer baselines. Comparison of individual model runs **suggests** than an “error bar” of approximately 0.5 dex effectively represents the rms fluctuations for comparison with the observations.

In practice, the models are run to match the characteristics of an individual **source**. The average correlated flux density on long baselines is specified to the model, either the Standard RSN model is specified or a value of $P(max)$ in terms of $P(SN1986J)$ is selected. The model then determines an RSN frequency necessary to reproduce the observed correlated flux density at u-v distances in excess of $10^6\lambda$. No formal goodness-of-fit is calculated, but the models are tightly constrained. As described in §4.2 the supernova rate varies over a very limited range for Starburst models. Values of $\nu_{sn} > 2yr^{-1}$ would appear to be excessive. Furthermore at large ν_{sn} the models are not a good fit to the observed visibilities because the large number of contributing RSN approximate a smooth source, and underpredict the correlated flux density on the longer baselines.

There are 11 galaxies with adequately sampled visibility functions such that we attempted RSN model fits to the data. Considerable care must be exercised in comparing the models to the observed visibility functions because the model averages substantially smooth the visibility functions on the longer baselines. Furthermore, the models contain only emission from relatively young RSN which fade before they become significantly extended. The observed visibility functions may include flux

density from extended emission which is not produced in our models. For this reason we do not exclude models which under-estimate the correlated flux density on short baselines. The “best fit” models, overplotted on the observed visibility functions are shown in Figure 6 and the model numerical results, compared with the “observational” data, are shown in Table 6. As described below, these are all luminous **RSN** models; in no case does a model with standard RSN provide an adequate fit.

Table 6, Column 2 gives the VLBI flux density from Table 2; this will generally be an upper limit to the model **VLBI** flux density, which corresponds only to the longest baselines. Column 3 lists the supernova frequency, ν_{sn}^{FIR} from Table 5, that is, the supernova frequency estimated by a Starburst model which reproduces the observed L_{FIR} . The gaussian model parameters are given in columns 4–7; these are respectively, the VLBI flux density for the model, S_{vlbi} as described above, the power of the model RSN in units of **RSN1986J**, P_{max}^{1986J} , the model supernova frequency, ν_{sn} , and ratio of the supernova frequency in our gaussian model fit to that calculated in the Starburst model. In column 8 we give an estimate of the quality of the model fit, as follows: **a** = ‘acceptable’, **m** = “fails in the midrange, otherwise acceptable”, **l** = “fails at low u-v distance, otherwise acceptable”, **p** = “poor”. An rough estimate of the number of supernovae visible at a given time — the number of RSN with flux densities greater than **20%** of the flux density at maximum light which, for the adopted decay rate, is the number of supernovae occurring within the last 10 years — may be obtained by multiplying the model ν_{sn} by ten.

The results of the clumped fits are shown in columns 9-17. Columns 9-12 provide the VLBI flux density, The RSN power at maximum, the supernova frequency and the supernova ratio as in the uniform gaussian models. Column 13 lists the total power of an RSN clump, P_{cl}^{1986J} , in units of **RSN1986J**; column 14 gives N_{cl} , the number of clumps which have detonated in the last 10 years; column **15** lists the number of supernovae per clump, $N_{sn}/cl = n_{sn} = P_{cl}/P_{sn}$ as described above; column 16 lists the clump diameter in parsecs; column 17 lists our assessment of the quality of fit.

There are no acceptable fits using “Standard RSN.” The large number of RSN required in these models to provide the flux density effectively washout any structure in the visibility function.

Furthermore the models require supernova frequencies many times the supernova frequency predicted by the Starburst models. We conclude that **Starbursts** with Standard RSN are incapable of producing the radio power and structure of the **LFIRGs**.

Among the luminous RSN models, none of the non-clumped gaussian models are **fully** acceptable representations of the observed visibility functions. Figure 6 and Table 6 show that most gaussian fits have too little correlated flux density on intermediate baselines (midrange). In one case, Arp 220, the gaussian model provides a marginally acceptable fit, depending upon the appropriate correlated flux density on longest **baselines**, where the observed visibility function is particularly variable. The failure of many of the models at baselines corresponding to a few pc at the typical LFIRG distances suggested that introducing clumps on such scales would provide a better fit to the visibility function. Clearly, the fact that GMC cores and globular clusters have sizes of a few pc provides scientific motivation for considering such models. As expected, the clumped models are generally a better fit. In all cases, the introduction of clumping improves the visibility function fit, and/or reduces other constraints such as RSN luminosity.

In summary:

1) Arp 220 is the only system which may plausibly be explained by a **Starburst/RSN** model without significant clumping. Since the date that these calculations were made, we have obtained strong evidence from VLBI imaging observations of Arp 220 that multiple, luminous RSN supply the **compact,milliarcsecond** scale radio emission that object (Smith *et al.* 1997). The structural characteristics of the Arp 220 image are a near perfect match to the Starburst model calculated in 4.2 with radio supernovae having luminosities and decay-times comparable to RSN1986J. This result is consistent with the recent ISO spectrophotometric observation that Arp 220 does not exhibit high-excitation mid-infrared features expected from a hard ionizing radiation field (Sturm *et al.* 1996).

2) For eight systems we judge that the clumped RSN models, with clump sizes from 2–10pc, provide an *acceptable fit* in terms of the general distribution of visibilities, the correlated flux density on long baselines, and the total flux density on scales smaller than 0! '25 due to RSN. This includes

Arp 220, plus 01173+1405, NGC 2623, UGC 4881, Mrk 273, NGC 6286, NGC 7469 and Mrk 331. The required luminosities of the **RSN**, particularly for **UGC 4881** and NGC 6286, are uncomfortably high. In these cases F'_{sn} is a factor of two or more greater even than that of Mrk 297a, assuming that this source is indeed a radio supernova.

3) Three systems, UGC 2369, UGC 5101, and Mrk 231, stand out as having extraordinary solutions: very large clump luminosity, small clump size, and high RSN luminosity. We judge the best RSN model fits to be unacceptable either because the visibility function is not well fit (UGC 5101) or because the required RSN luminosity is too great by more than an order of magnitude (**UGC 2369 & Mrk 231**). In our estimation, these galaxies *must* harbor AGN radio cores. VLBI imaging observations of three systems (**Lonsdale et al. 1997**) confirm this hypothesis for Mrk 231 and UGC 5101 and suggest that the **Sy1.5** galaxy, NGC 7469, also harbors a radio AGN. Mrk 231, UGC 5101 and NGC 7469 are the highest excitation galaxies in the sample and would be the chief AGN candidates based upon other characteristics, including emission-line spectrum and infrared characteristics.

4) The uniform characteristic of the acceptable RSN model fits is that they require multiple, luminous RSN like **SN1986J** to fit the **LFIRG** visibility functions regardless of the assumed supernova frequency. Even allowing the supernova frequency to exceed our Starburst model calculations by large factors, normal RSN cannot reproduce the observed visibility functions because the number of normal RSN required to produce the observed flux-density cannot reproduce the observed structure. Furthermore, the acceptable solutions suggest that RSN are likely to be clumped on pc scales. As described above, the requirement that spatial clumping contribute structure in the visibility function at intermediate scales implies that the supernovae within a given clump must detonate within **timescales** of a few years. This is a remarkable conclusion; how such “chain-reactions” of RSN may be triggered is a challenging theoretical problem.

It is worth asking whether any of the other galaxies in our sample (i.e. those with sparse VLBI detections or upper-limits to S_{vlbi}) have limits on compact, **VLBI-scale** flux density ($S_{\text{vlbi}}^{\text{max}}$ in Table 1) which would be exceeded by luminous RSN at the calculated supernova rate. In fact, the rest of

our sample is fully consistent with the inference that compact, **luminous** Starbursts are dominated by luminous RSN on **milliarcsecond** scales.

5. CONCLUSIONS

To summarize the conclusions of this work:

1. Luminous **FIR** galaxies have radio emission which exhibits structure on a large range of scales, typically a few **mas** to several tenths of an **arcsecond**.
2. The VLBI power in **LFIRGs** is weakly correlated with infrared luminosity, total **1.49GHz** radio power, radio spectral index, and molecular gas mass (CO luminosity). These correlations suggest a physical relationship among these quantities which may be interpreted in terms of Starburst or hybrid (Starburst plus AGN) models.
3. Given the wealth of structures associated with compact, **nonthermal** radio emission in AGN, the observed radio data are easily **accommodated** by AGN **models**. Combined with the analysis of **LSL95**, a plausible case may be made for **LFIRGs** as dust-enshrouded **AGN**.
4. Starburst models for **LFIRGs** are extreme, with very high star-formation ratea and luminous energy densities, but plausible, in terms of providing the FIR luminosity and other global characteristics of **LFIRGs**. Simple **modelling** infers star-formation rates ranging from **15–200 $M_{\odot}yr^{-1}$** and an associated supernova frequency, $\nu_{sn} \sim \frac{1}{2}–2yr^{-1}$
5. Starburst-generated radio supernovae may be responsible for the compact, **milliarcsecond**-scale radio structures in many, but not all, of our **LFIRG** sample galaxies. Notable exceptions are Mrk 231 and UGC 5101. Models which adequately reproduce the 18cm **LFIRG** visibility functions require multiple, highly-luminous radio supernovae.
6. In most successful Starburst/RSN models the RSN must detonate in clumps of scale 2-10pc and, inside a given clump, multiple supernovae must detonate within **timescales** of a few years.

The firm conclusion from this work is that, in those systems dominated by Starburst activity, nearly every supernova explosion results in a luminous radio supernova, with power comparable to or greater than RSN 1986J. As described above, reasonable choices for the IMF in starburst galaxies will lead to supernovae with intermediate mass progenitors, so it does not appear plausible to appeal to a new supernova mechanism (e.g. from a supermassive star) which provides a greater store of kinetic energy to accelerate particles and amplify magnetic field in the **LFIRGs**. The form of the light curves (Weiler *et al.* 1990) suggest that the external medium into which the plasma expands may be somewhat different in luminous RSN from that for standard RSN, in that a dense ambient medium may be combined with a synchrotrons emitting medium. Still, the densities inferred for the compact star-formation regions in **LFIRGs** are similar to those for GMCS and for the winds postulated to emanate from the RSN progenitor. Recent work suggests that the geometry of the molecular regions may be the most significant environmental difference (Scoville, Yun and Bryant 1997) with the warm molecular material confined to thick disk-like structure in the compact **LFIRGs**. In this case, it is possible that stronger, more highly ordered magnetic fields may provide the conditions appropriate for such luminous RSN. Polarization observations would be a useful discriminant if this is the case,

For some time it has seemed likely that active star-formation and AGN activity coexist in Luminous FIR Galaxies; the question is then to assess the relative contribution from each form of activity to the energetic of the system and to determine from the sample systematic if, as appears likely, there is a physical relationship between the Starburst and AGN or perhaps an evolutionary progression from one to the other. LSL95 used the compact-radio/infrared characteristics of our sample to establish plausibility that AGN activity could be responsible for the bulk of the luminosity in our **LFIRG** sample. The **Starburst/RSN** models presented here provide a similar case for Starburst activity.

Until our imaging observations of Arp 220 (Smith *et al.* 1997), we had considered the requirement that **LFIRGs** exhibit multiple, extremely luminous RSN at the rate of order one-per-year to be sufficiently extreme that the existence of AGN cores remained the most likely interpretation of

the VLBI observations. AGN radio cores are almost certainly present in UGC 2369, Mrk 231, UGC 5101, and NGC 7469, but multiple, luminous RSN are with **equal** certainty present in Arp 220. Thus, the RSN models for the other systems, most with lower supernova frequency than Arp 220, must be considered quite plausible. With recent evidence that active star formation is occurring via formation of globular clusters or “super star clusters” (Ho 1996) the clumping suggested by our RSN models is easily accommodated. The range of clump size, 2-10PC is well within the range of core radii for Galactic globular clusters, $r_c \sim 0.2\text{--}15\text{pc}$ (Peterson & King 1976).

In two systems, Arp 220 and Mrk 231, there is sufficient evidence to point to a dominant overall energy source, Starburst for the former, AGN for the latter. Our evidence suggests that NGC 7469 houses an AGN radio core, but this **Sy1.5** galaxy also shows a **circumnuclear** Starburst (Wilson *et al.* 1991, Miles, Houck & Hayward 1994, Mozzarella *et al.* 1994) which is likely to dominate at mid-FIR wavelengths (Jones *et al.* 1997) and thus provide the dominant energy source. If we assume that all **LFIRGs** with acceptable Starburst fits are indeed Starbursts, a supposition that is by no means proven, we have potentially six Star burst systems, three possible hybrid/intermediate systems, and one quasar. A **Starburst-AGN** evolutionary interpretation of such a picture would suggest that the Starburst phase is relatively long lived and that the radio AGN “turns on” significantly before the AGN dominates at other wavelengths, perhaps as the late-stage Starburst begins to fuel the coalescing central compact object (Norman & Scoville 1988) or the supernovae interact with the nascent AGN (Perry & Dyson 1985). Numerical simulations of mergers like those believed to give rise to” **LFIRGs** suggest that the onset of the Starburst occurs relatively late in the merger process (Mihos & Hernquist 1996), $\tau \sim 10^8 \text{yr}$, and our results suggest that the Starburst may carry on for another 10^8yr as the nuclei merge and an AGN forms. Once the AGN fully turns on, it must shed its shroud of dust relatively quickly, perhaps extinguishing the star formation in the process, as must be the case to account for the large store of molecular gas in Mrk 231, the only true dust-enshrouded quasar in the above picture.

Much work remains to be done to establish the nature of the relationship between the Starburst and AGN activity in I, FIRGs. Our statistical analysis of the **LFIRG** sample demonstrates that the

physical relationship or evolutionary sequence is not straightforwardly evident from the **global** sample characteristics, but must be elucidated from careful study of individual objects. Further VLBI maser and continuum imaging observations, as well as mid-Infrared imaging and spectroscopy are planned for this sample.

The authors wish to acknowledge Joe Mozzarella for helpful discussions of optical spectra and for providing tabulated data on our sample galaxies. We have benefitted from illuminating discussions with Dave Sanders and Wayne Stein. Thanks to Barry Madore for pointing us to distance information for the NGC 1023 Group, to the staff of Lick Observatory for support of optical observations, and to Haystack Observatory for hospitality. HES wishes to express deep gratitude to IPAC for providing continued support as a home away from home. This project has benefitted from the use of NED — the NASA Extragalactic Database — supported at IPAC by NASA. IPAC/JPL is supported by NASA. Haystack is supported by the NSF via NEROC. Support of this project at UCSD has been provided by the NSF under grant **AST93-19895**.

REFERENCES

- Armus, L., Heckman, T., & Miley, G. 1989, ApJ, 347, 727.
- Baldwin, J. A., Phillips, M. M., & Terlevich, R., 1981, PASP, 93, 5.
- Bryant, P. M., & Scoville, N. Z. 1996, ApJ, 457, 678.
- Chevalier, R. A. 1982, ApJ, 259, 302.
- Ciardullo, R., Jacoby, G., & Harris, W. 1991, ApJ, 383, 487.
- Chini, R. Krugel, E., & Steppe, H. 1992, A&A, 255, 87.
- Condon, J. J., Anderson, M. L., & Helou, G. 1991, ApJ, 376, 95.
- Condon, J. J., Huang, Z.-P., Yin, Q. F., & Thuan, T. X. 1991, ApJ, 378, 65 (CHYT).
- Condon, J. J., & Yin, Q. F. 1990, ApJ, 357, 97.
- Diamond, P., Lonsdale, C. J., Lonsdale, C. J., & Smith, H. E. 1997, *in preparation*.
- Granato, G. L. & Danese, L. 1994, MNRAS, 268, 235.
- Granato, G. L., Danese, L., & Francheschini, A. 1996, ApJ, 460, L11.
- Ho, L. C. 1996 in *Starburst Activity in Galaxies*, J. Franco, R. Terlevich, G. Tenorio-Tagle, eds.,
Rev. Mex. Astr. Astrofis., , *in press*.
- Isobe, T., Feigelson, E. D., & Nelson P. I. 1986, ApJ, 306, 490.
- Jones, B., Puetter, R., Smith, H. E., & Stein, W. 1997, *in preparation*.
- Jones, T. W. & Kang, H. 1993, ApJ, 402, 560.
- Leitherer, C. & Heckman, T. 1995, ApJS, 96, 9.
- Lonsdale, C. J., Diamond, P., Smith, H. E., & Lonsdale, C. J. 1994, *Nature*, 370, 117.
- Lonsdale, C. J., Diamond, P., Smith, H. E., & Lonsdale, C. J. 1997, *in preparation*.
- Lonsdale, C. J., Lonsdale, C. J., & Smith, H. E. 1992, ApJ, 391, 629 (LLS92).
- Lonsdale, C. J., Lonsdale, C. J., Diamond, P. D. & Smith, H. E. 1997, *in preparation*.
- Lonsdale, C. J., Smith, H. E., & Lonsdale, C. J. 1993, ApJ, 405, L9 (Paper I).

- Lonsdale, C. J., Smith, H. E., & Lonsdale, C. J. 1995, *ApJ*, 438, 632 (LSL95).
- Low, F. J., **Huchra**, J., **Kleinmann**, S. 1988 *ApJ*, 327, L41.
- Low, F. J., **Cutri**, R., **Kleinmann**, S., & **Huchra**, J. 1989, *ApJ*, 340, L1.
- Mozzarella, J. M., Voit, G. M., Soifer, B. T., Matthews, K., Graham, J., Armus, L., & Shupe, D. 1994, *AJ*, 107, 1274.
- Mihos, J. C. and Hernquist, L. 1996, *ApJ*, 464, 641.
- Miles, J. W., **Houck**, J. R., & Hayward, T. L., 1994, *ApJ*, 425, L37.
- Miller, J. & Scale, J. 1979, *ApJS*, 41, 513.
- Mirabel**, I. F., Booth, R., **Garay**, G., **Johansson**, L., & Sanders, D. 1990, *A&A*, 236, 327.
- Norman, **C.** & **Scoville**, N. 1988, *ApJ*, 332, 124.
- Norris, R. P., Allen, D., Sramek, R., Kesteven, M., & Troup, E. 1990, *ApJ*, 359, 291.
- Perry, J. J., & Dyson, J. E. 1985, *MNRAS*, 213, 665.
- Peterson, C., & King, I. 1976, *AJ*, 80427.
- Pier, E. A. & **Krolik**, J. 1992, *ApJ*, 401, 99.
- Pier, E. A. & **Krolik**, J. 1992, *ApJ*, 418, 673.
- Polatidis**, A. G., Wilkinson, P. N., Xu, W., Readhead, A. C. S., Pearson, T. J., Taylor, G., & **Vermuelen**, R. 1995, *ApJS*, 98, 1.
- Rowan-Robinson, M. 1995, *MNRAS*, 272, 737.
- Sanders, D. B. & **Mirabel**, I. F. 1996, *ARA&A*, 34, 749.
- Sanders, D. B., Soifer, B. T., **Elias**, J., Madore, B., Mathews, K., Neugebauer, G., & **Scoville**, N. 1988, *ApJ*, 325, 74.
- Sanders, D. B., **Scoville**, N. Z., & Soifer, B. T. 1991, *ApJ*, 370, 158.
- Schmidt, M. & Green, R. F. 1983, *ApJ*, 269, 352.
- Scoville**, N. Z., Sargent, A. I., Sanders, D. B., & Soifer, B. T. 1991, *ApJ*, 366, 1,5.

- Scoville, N. Z. & Soifer, B. T. 1991, in *Massive Stars in Starbursts*, ed. Leitherer, C., Walborn, N. Heckman, T. & Norman, C. [Cambridge Univ. Press: Cambridge, UK], p. 233.
- Scoville, N. Z., Yun, M. S., & Bryant, P. M. 1997, ApJ, *in press*.
- Silberman, N. A., *et al.* 1996, ApJ, 470, 1.
- Smith, H. E., Lonsdale, C. J., Lonsdale, C. J., & Diamond, P. D 1997, submitted to the ApJ.
- Soifer, B. T., Boehmer, L., Neugebauer, G., & Sanders, D. B. 1989, AJ, 98, 766.
- Solomon, P., Dowries, D., & Radford, S. 1992, ApJ, 387, 1.55.
- Solomon, P., Downes, D., Radford, S., & Barrett, J. 1997, ApJ, *in press*.
- Spinoglio, L. & Malkan, M. 1992, ApJ, 399, 504.
- Sturm, E., *et al.* 1996, A&A, 316, L133.
- Terlevich, R. & Melnick, J. 1985, MNRAS, 213, 831.
- Thakkar, D. D., Xu, W., Readhead, A. C. S., Pearson, T. J., Taylor, G., Vermuelen, R., Polatidis, A. G., & Wilkinson, P. N., 1995, ApJS, 98, 33.
- Veilleux, S., Kim, D.-C., Sanders, D. B., Mozzarella, J. & Soifer, B. T. 1995, ApJS, 98, 171.
- Veilleux, S. & Osterbrock, D. E. 1987, ApJS, 63, 295.
- Voit, G. M. 1992, ApJ, 399, 495.
- Weiler, K. W., Panagia, N., & Sramek, R., 1990, ApJ, 364, 411.
- Weiler, K. W., Sramek, R., Panagia, N., van der Hulst, J., & Salvati, M., 1986, ApJ, 301, 790.
- Wilkinson, P. N., & de Bruyn, A. G. 1990, MNRAS, 242, 529.
- Wilson, A. S., Heifer, T. T., Haniff, C. A., & Ward, M. 1991, ApJ, 381, 79.
- Xu, W., Readhead, A., Pearson, T., Polatidis, A., & Wilkinson, P., 1995, ApJS, 99, 297.
- Yin, Q. F., & Heeschen, D. S. 1991, *Nature*, 354, 130.

Fig. 1.— Visibility plots for the 16 sources with detections on at least two VLBI baselines and estimated $T_b \gtrsim 10^6 K$. Error bars are 1σ representing a combination of thermal noise and estimated calibration error. The three curves -- $10^5 K$, $10^6 K$ and $10^7 K$ for the solid, dashed and dotted lines respectively, represent the correlated flux density for a source of the given brightness temperature, assuming a circular gaussian source shape with FWHM 0.5 times the fringe spacing.

Fig. 2.— Histograms of VLBI power for detected (lower panel) and non-detected (upper panel) galaxies in our LFIRG sample.

Fig. 3.— VLA-A Array images at 22 GHz and 15 GHz for 14 luminous infrared galaxies. Each source is displayed in four panels with varying angular resolution and sensitivity resulting from differing u-v weighting methods. Each panel is $1''4$ on a side. Below each set of four panels is a set of **minipanel**s, in each of which are listed the key parameters of the corresponding image. On the first line, a “K” indicates 22 GHz, and “U” indicates 15 GHz. The u-v plane weighting method used is uniform (highest resolution, inferior sensitivity), natural (lower resolution, maximum sensitivity) and tapered (much lower resolution, better surface-brightness sensitivity). The restoring beam size in **milliarcseconds**, and the position angle of its major axis are given on the next line, and on the last line the contour interval is given in mJy. The **B1950.0** coordinates of the field center are given to the right of the minipanel. Also to the right of the **minipanel**s are two ellipses. The open ellipse is the FWHM of the CHYT restoring beam for that source, and the solid ellipse is the deconvolved size derived by CHYT, with position angle estimated from the 8.4 GHz images, both on the same angular scale as our K and U band images. This is intended to provide a point of reference for assessing the substructure revealed by our images.

Fig. 4.— Excitation diagram for the sample. The solid line represents the boundary between thermal and **nonthermal** excitation (Veilleux & Osterbrock 1997). Two broad-line objects with positive detections, Mrk 231 and NGC 7469, have been omitted. VLBI detections with high brightness temperature are plotted with an asterisk; detections with $T_b \sim 10^5 - 10^6 K$ are plotted as a plus; non-detections are open circles. While most galaxies with AGN-like optical spectra show compact high- T_b emission, excitation is not a good indication of the presence of compact VLBI emission.

Fig. 5.— Synthetic visibility functions for **RSN/Starburst LFIRG** models. The **galaxy** is assumed to be at a distance of 100Mpc, with supernova rate $\nu_{sn} = 1 \text{ yr}^{-1}$ calculated to produce a VLBI flux density, $S_{vlbi} = 2 \text{ mJy}$ and total flux density 30mJy. Panel (a) shows the variation the visibility function with RSN luminosity for a gaussian (non-clumped) model. Clumped models are shown in panels (b) — (d). The fiducial model has eight supernovae per clump, $N_{sn}/cl = 8$, detonated simultaneously with $P_{cl} = 8 \times P^{1986J}$, hence $P_{sn} = 1.0 \times P^{1986J}$, in clumps with size, $d_{cl} = 4.0 \text{ pc}$. The effect of varying clump power, P_{cl} is shown in panel (b); in this case the number of RSN per clump is kept constant ($N_{sn}/cl = 8$), thus the individual RSN power also scales. Panel (c) shows the effect of varying the clump size. Finally, panel (d) shows the effect of the degree of clumping: clump luminosity is adjusted as number per clump was varied, maintaining constant RSN luminosity. Thus, we have a series of models with similar RSN which get progressively clumpier in their spatial distribution. The curves are labelled by N_{sn}/cl .

Fig. 6.— Synthetic visibility function fits for 11 **LFIRGs**; model parameters are given in Table 6. In each case the observed visibility function is the heavy solid line; the dotted curve is our “best fit” gaussian (**unclumped**) model; the dashed curve represents the best clumped model. Because many individual visibility functions are averaged to produce the models, the models are smoother on long baselines compared to the actual visibility functions. A typical rms fluctuation of about 0.5 dex is appropriate for comparison of model with observation.

TABLE 1
I, UMINOUS FIR GALAXY SAMPLE

SYSTEM	RADIO POSITION		D (Mpc)	$\log M_{H_2}^{\dagger}$ (M_{\odot})	$\log L_{FIR}$ (L_{\odot})	IRAS DATA				RADIO DATA		
	α (1950)	δ				S_{12}	S_{25} (Jy)	S_{60}	S_{100}	$S_{1.49}$ (mJy)	$\alpha_{1.49}^{\ddagger}$	S_{ν}^{max} (mJy)
(1)	(2)	(3)	(4)	(5)	(6)	(7)	(8)	(9)	(10)	(11)	(12)	(13)
Mrk 938	000833.40	-122308.9	77	9.46 [§]	11.28	0.36	2.38	16.08	16.97	68.7	0.78	21.3
IC 1623 ¹	01 0519.9	-174626	71	10.44	11.39	0.98	3.43	2219	30.32	211.		4.7
01076-1707	01 0741.22	-170707.3	131	10.30 [†]	11.42	0.47	0.88	6.76	10.20	41.9	0.70	1.2
01173+1405	01 1723.17	+14 0558.7	124		11.54	0.27	1.41	10.72	9.60	43.1	0.70	8.4
01364-1042	01 3624.27	-104224.3	187	10.18 [†]	1.67	<0.15	0.43	6.53	7.00	17.0	0.42	12.7
111 Zw 035	01 4147.91	+16 6106.3	109	9.84	1.46	<0.10	1.00	11.86	13.75	39.3	0.40	26.3
NGC 695	014827.85	+22 2006.9	130	10.34	1.51	0.49	0.81	7.61	13.80	67.6	[0.88]	1.2
UGC 2369	0251 15.92	+14 4603.9	124		1.42	0.22	1.75	7.68	11.10	42.7	0.67	11.3
03359+1523	033558.33	+15 2309.4	140	10.37	1.37	<0.12	0.57	5.77	6.53	18.9	0.31	8.8
04191-1855	04 1906.95	-185541.9	123		1.34	0.23	0.55	5.84	10.04	27.3	0.65	14.7
	04 1907.1	-185600										
NGC 1614 ²	043135.7	-084057.2	61	10.03	1.39	1.44	7.82	33.12	36.19	107.	[1.05]	
05189-2524	051858.88	-252439.4	166	10.37	1.91	0.74	3.50	13.95	12.52	28.1	0.52	18.9
NGC 2623	083525.27	+25 55 50.2	76	9.77	1.47	0.24	1.85	25.72	27.36	97.8	0.58	31.8
08572+3915	085712.96	+39 1538.9	236	9.78 [†]	1.96	0.34	1.84	7.66	5.06	6.5	0.27	5.6
UGC 4881	091238.43	+44 3229.2	163	10.46	11.61	0.16	0.62	6.53	10.21	29.0	0.69	13.8
UGC 5101	093204.78	+61 3437.0	164	10.32 [†]	11.93	0.26	1.08	13.03	21.25	146.	0.59	85.1
10173+0828	101722.26	4-082839.7	194	10.35	11.70	<0.11	0.67	6.08	5.97	8.8	0.28	7.7
10566+2448	105636.17	+24 4839.9	170	10.34	11.90	0.21	1.21	12.63	16.06	46.1	0.68	7.8
11010+4107	110105.81	+41 07 10.s	142	10.18	11.82	0.12	0.37	6.95	10.99	28.0	0.55	13.7
UGC 6436	112308.6	+14 5706	139	10.26	11.44	<0.13	0.68	5.60	9.80	22.0	(0.82)	3.8
	11 2313.1	+14 6637										
Mrk 171 ³	112544.19	+58 5018.2	48	10.06	11.74	3.90	24.14	122.	122.	658.	[0.67]	86.2
	11 2541.53	+58 5012.4										
12112+0305	12 11 12.48	+03 0522.1	292	10.62	12.18	<0.14	0.52	8.39	9.10	22.6	0.47	13.5
	12 11 12.37	+03 0519.7										
Mrk 231	125405.01	+57 0838.2	173	10.19	12.35	1.93	8.80	35.40	32.28	240.	-0.06	225.
Arp 238	13 1341.s3	+62 2317.9	130	10.13	11.62	0.35	1.96	12.01	12.92	51.2	0.64	8.2
	131337.5	+62 2335										
13183+3424	131817.01	+34 2404.7	97	9.87	11.61	0.26	1.37	13.69	24.90	106.	0.64	13.3
Mrk 266	1996 15.01	+48 51 54.1	116	10.15	11.34	0.28	1.13	7.19	10.35	98.8	0.64	11.9
	133614.46	+48 3145.2										
	133614.8	+48 3149										
NGC 5257	133719.6	+01 0535	95		11.37	0.62	1.47	10.68	18.69	47.8		1.2
NGC 5258	133719.64	+01 0523.3										
Mrk 273	134251.71	+56 0814.9	1s7	10.24	12.04	0.23	2.30	22.09	22.44	130.	0.63	56.5
	134261.76	+56 0813.6										
14348-1447	143453.30	-144726.1	326	10.78	12.17	<0.12	0.56	6.46	6.92	33.2	0.71	13.6
UGC 9618	145448.24	+24 4903.9	140		11.58	0.36	0.47	6.68	14.54	68.8	[0.60]	1.9
Mrk 848	151619.30	+42 5538.3	166	10.27	11.72	0.22	1.40	9.15	10.04	46.8	0.78	14.9
	161619.61	+42 5531.3										
15250+3608	152503.72	+36 0901.0	219		11.88	0.12	1.28	7.20	5.78	12.8	0.11	11.6
Arp 220	153246.88	+23 4007.9	78	10.28	12.11	0.64	7.92	103.	114.	301.	0.41	91.2
	153246.95	+23 4007.7										
NGC 6090	161024.58	+52 3505.4	122	10.15	11.33	0.29	1.22	6.25	9.34	48.3		1.2
NGC 6286 ⁴	165744.99	+59 0041.7	80	9.97	11.27	0.50	0.64	9.87	22.01	142.	[0.84]	22.7
17132+5313	171313.49	+53 1349.3	208	10.55	11.79	0.12	0.66	6.35	8.44	28.4	0.67	5.4
22491-1808	224909.09	-180820.6	302	10.43	12.02	<0.09	0.56	5.28	4.58	6.1	0.41	5.1
NGC 7469	230044.41	+08 3615.8	66	9.96	11.41	1.60	5.84	27.68	34.91	183.	0.68	36.3
Zw 475.056	231333.13	+25 1701.6	111	9.98	11.37	0.32	1.88	8.75	11.64	26.0	0.67	11.3
Mrk 331	234854.03	+20 1829.2	72	10.11	11.27	0.51	2.56	17.32	20.86	67.5	0.66	20.5

[§] Molecular hydrogen masses are from CO observations by Sanders, Scoville & Soifer (1991).

[§] H_2 mass from Chini, Krugel & Steppe (1992).

[†] H_2 mass from Mirabel *et al.* (1990).

[†] H_2 mass from Solomon *et al.* (1997).

¹The companion, IC1622, 3' SW, accounts for less than 3% of the radio flux density at 1.49 GHz (Condon *et al.* 1990) suggesting that IC 1623 dominates the IRAS infrared measures.

²Radio position at 1.49 GHz (Condon *et al.* 1990).

³Mrk 171 = NGC 3690/IC694. Sources D and B from Condon *et al.* 1990, corresponding to the nuclei of IC 694 and NGC 3690, respectively.

⁴The IRAS position agrees with the position of NGC 6586 from the interacting pair Arp 293 = NGC 6285/6. Surace *et al.* 1993, have deconvolved the pair at 12, 25 and 60 μm , showing that the bulk of the FIR flux density originates from NGC 6586, as does over 90% of the 1.49 GHz flux density. This source is incorrectly listed as NGC 6285 in Paper I.

TABLE 2
VLBI RESULTS

SOURCE	$S_{1.49}$ (mJy)	$\log P_{1.49}$ (W/H z)	q	S_{vlbi} (mJy)	$\log P_{\text{vlbi}}$ (W/H z)	$\log T_b^1$ (K)
(1)	(2)	(3)	(4)	(5)	(6)	(7)
Mrk 938	58.7	22.62	2.52	< 2.5	<21.25	5.0†
01173+1405	43.1	22.93	2.46	7.0	22.11	>>7§
01364-1042	17.0	22.85	2.67	< 2.0	<21.92	< 5
III Zw 035	39.3	22.74	2.57	< 1.0	<21.15	5.4†
UGC 2369	42.7	22.89	2.38	15.	22.44	>>7§
03359+1523	18.9	22.64	2.58	3.0	21.85	>> 7*
04191-1855	27.3	22.69	2.49	< 2.5	<21.65	< 5
05189-2524	28.1	22.96	2.76	< 3.0	<21.99	< 5
NGC 2623	97.8	22.83	2.50	9.0	21.79	>>7§
08572+3915	6.5	22.64	3.10	<1.5	<22.00	< 5
UGC 4881	29.0	22.96	2.49	4.0	22.10	>> 7*
UGC 5101	146.	23.66	2.10	28.	22.95	>>7§
10173+0828	8.8	22.60	2.91	3.6	22.21	6.1†
11010+4107	28.0	22.83	2.54	<1.5	<21.56	5.1†
Mrk 171D	658.	23.25	2.34	1.5	20.61	>> 7*
12112+0305	22.6	23.36	2.66	<1.3	<22.12	< 5
Mrk 231	240.	23.93	2.23	115	23.61	>>7§
Arp 238	51.2	23.01	2.45	< 1.5	<21.48	< 5
13183+3424	106.	23.07	2.28	< 0.9	<21.00	< 5
Mrk 266	98.8	23.20	1.99	4.5	21.86	6.4*
Mrk 273	130.	23.58	2.31	16.0	22.67	>>7§
14348-1447	33.2	23.62	2.37	< 2.5	<22.50	< 5
Mrk 848	46.8	23.18	2.38	3.5	22.06	7.5*
15250+3608	12.8	22.86	2.80	6.5	22.57	6.2*
Arp 220	301.	23.34	2.62	10.5	21.88	>>7§
NGC 6286	142.	23.03	2.05	13.0	22.00	7.0§
17132+5313	28.4	23.17	2.46	< 1.5	<21.89	< 5
22491-1808	6.1	22.85	2.90	< 4.0	<22.64	5.2†
NGC 7469	183.	22.98	2.29	12.0	21.79	>> 7§
ZW 475.056	26.0	22.58	2.64	< 0.8	<21.07	< 5
Mrk 331	67.5	22.62	2.51	7.5	21.67	>>7§

¹ Symbols indicate structure in visibility plot; * = *simple*, § = *complex*, † = single baseline detection.

TABLE 3
SPECTROPHOTOMETRIC DATA

Object	$\log L_{H\alpha}$ (erg s^{-1})	$\frac{[OIII]}{H\beta}$	$\frac{[NII]}{H\alpha}$	$\frac{[SII]}{H\alpha}$	$\frac{[OI]}{H\alpha}$	Spectral Type	Ref. ¹
(1)	(2)	(3)	(4)	(5)	(6)	(7)	(8)
Mrk 938	42.93	0.50	0.10	-0.33	-0.93	sy2	d
IC 1623N	41.43	0.10	-0.56	-0.59	-1.43	H II	d
IC 1623SE	41.72	0.36	-0.67	-0.63	-1.66	H II	d
01076-1707	42.48	-0.42	-0.29	-0.66	-1.61	H II	d
01173+1405	...	0.10	-0.43	-0.56	-1.30	H H	c
01173+1405	42.02	-0.06	-0.41	-0.54	-1.36	H II	d
01364-1042	...	0.3	-0.05	AGN	c
01364-1042	41.22	0.21:	-0.02:	-0.23:	-0.46:	Liner	d
111 Zw 035	...	0.	0.10	-0.23	-0.67	H H	c
III Zw 035S	41.36	0.07;	0.01	-0.31	-0.68	Liner	d
III Zw 035N	40.70	0.28	-0.72	-0.52	-1.33	H II	d
NGC 695	41.88	-0.55	-0.35	-0.80	-1.23	H II	d
UGC 2369	42.26	-0.40	-0.28	-0.67	-1.65	H H	d
03359+1523	41.97	0.03	-0.46	-0.72	-1.70	H II	d
04191 -1855S(a)	41.51	-0.51	-0.11	-0.45	-1.11	Liner:	d
04191 -1855N(b)	41.48	-0.22	-0.20	-0.44	-0.98	Liner	d
NGC 1614	42.67	-0.17	-0.22	-0.72	-1.73	H H	d
05189-2524	42.94	1.5:	0.03	-0.72	-1.12	sy2	d
NGC 2623	40.73"	...	-0.01	-0.22	-0.99	AGN	d
08572+3915	40.88	0.25	-0.38	...	-1.13	H II	a
08572+3915	41.29	0.31	-0.38	-0.39	-1.28	Liner:	d
UGC 4881	...	0.	-0.19	H II	c
UGC 4881 NE(b)	42.21	-0.55:	-0.15	-0.56	-1.24	H II:	d
UGC 4881 SW(a)	42.53	-0.33	-0.20	-0.54	-1.26	H II:	d
UGC 5101	43.10	0.36	0.12	-0.45	-0.95	Liner	d
10173+0828	39.93		a
10566+2448	43.05	-0.30	-0.32	-0.59	-1.38	H II	d
11010+4107	...	0.19	-0.33	H II	c
UGC 6436 NW(a)	42.74	-0.53	-0.32	-0.74	-1.54	H II	d
UGC 6436SE(b)	42.59	...	-0.24	-0.69	-1.55:	AGN	d
Mrk 171D	...	-0.05	-0.34	-0.50	-1.24	H II	b
12112+0305	40.84	0.28	-0.30	-0.30	-0.95	H II	a
Mrk 231	42.30	Syl	
Arp 238	41.7	0.04	-0.38	-0.67	-1.49	H II	a
Arp 238SE(b)	42.33	-0.01	-0.39	-0.67	-1.45	H II	d
Arp 238 NW(a)	41.68	0.11	-0.34	-0.46	-1.22	H II:	d
13183+3424	...	-0.7	-0.16	H II	c
13183+3424	41.82	-0.16	-0.18	-0.40	-0.94	Liner	d

TABLE 3—Continued

Object	$\log L_{H\alpha}$ (erg s^{-1})	$\frac{[OIII]}{H\beta}$	$\frac{[NII]}{H\alpha}$	$\frac{[SII]}{H\alpha}$	$\frac{[OI]}{H\alpha}$	Spectral Type	Ref. ¹
(1)	(2)	(3)	(4)	(5)	(6)	(7)	(8)
Mrk 266	...	0.15	−0.22	H II	a
Mrk 266 NE(c)	41.77	0.62	−0.25	−0.44	−1.25	sy2	d
Mrk 266 SW(a)	41.45	0.14	−0.20	−0.33	−0.91	Liner	d
NGC 5257	40.65	−0.12	−0.46	−0.57	−1.67	H II	d
NGC 5258	−0.25		d
Mrk 273	41.64	0.64	−0.06	−0.29	−0.90	AGN	a
Mrk 273	42.37	0.45	0.01	−0.24	−0.85	Liner	d
14348–1447	...	0.	−0.25	−0.39	−1.26	AGN	a
14348–1447SW(a)	42.74	0.13	−0.23	−0.48	−1.02	Liner	d
14348–1447NE(b)	41.88	0.09	−0.21	−0.51	−0.85	Liner:	d
UGC 9618	40.94	−0.06	−0.09	−0.46	−1.10	Liner	d
Mrk 848	41.7	−0.06	−0.33	H II	a
Mrk 848N(a)	42.44	−0.04	−0.26	−0.59	−1.42	H II	d
Mrk 848S(b)	42.32	−0.06	−0.12	−0.35	−1.07	Liner	d
15250+3608	41.03	0.79	−0.32	−0.39	−1.04	AGN	a
15250+3608	41.82	0.11	−0.33	−0.45	−1.13	Liner:	d
Arp 220	40.53	0.20	0.36	−0.13	−0.79	AGN	a
Arp 220W	0.29	−0.04	−0.70	AGN	d
Arp 220E	...	0.79	0.22	−0.16	−0.62	sy2	d
NGC 6090NW “	42.29	−0.35	−0.48	−0.79	−1.74	H II	d
NGC 6090SE	41.72	0.08	−0.46	−0.65	−1.73	Liner	d
NGC 6285	41.12	−0.33	−0.32	−0.29	−1.24	H II	d
NGC 6286	40.91	−0.25	−0.08	−0.18	−0.81	Liner	d
NGC 6286	...	−0.14	−0.39	H II	c
17132+5313W	−0.47	−0.22	...		d
17132+5313E	41.59	−0.38	−0.35	−0.50	−1.63	H II	d
22491–1808	42.29	−0.19	−0.37	−0.62	−1.24	H II	d
NGC 7469	42.17	−0.28	−0.74	−1.34	−2.02	Syl	d
Zw 475.056	...	0.38	−0.02	AGN	c
Zw 475.056	42.02	0.62	−0.02	−0.59	−1.26	sy2	d
Mrk 331	...	−0.45	−0.25	−0.66	−1.66	H II	c
Mrk 331	42.15	−0.46	−0.27	−0.60	−1.55	H II	d

¹References: a) Armus, Heckman & Miley; b) LSL92; c) This work; d) Veilleux *et al.* (1994).

TABLE 4
COX-HAZARD CORRELATION TESTS FOR THE **LFIR** SAMPLE

Independent Variable (1)		Dependent Variable (2)	# Data Points (3)	# Limits (4)	Upper (5)	χ^2 P (6)
L_{FIR}	Vs.	P_{vlbi}	31	14	3.1	0.08
		P'_{vlbi}			3.8	0.05
		$\frac{P_{vlbi}}{P_{tot}}$			0.10	0.75
P_{tot}	Vs.	P_{vlbi}	31	14	6.6	0.01
[25/60]	vs.	P_{vlbi}	31	14	0.02	0.88
		P'_{vlbi}			0.06	0.81
		$\frac{P_{vlbi}}{P_{tot}}$			0.24	0.62
[60/100]	vs.	P_{vlbi}	31	14	0.00	0.99
		P'_{vlbi}			0.24	0.62
		$\frac{P_{vlbi}}{P_{tot}}$			0.06	0.80
C_{60}	Vs.	P_{vlbi}	31	14	0.05	0.82
		P'_{vlbi}			0.02	0.90
		$\frac{P_{vlbi}}{P_{tot}}$			0.21	0.65
$\alpha_{1.49}^{8.44}$	Vs.	P_{vlbi}	31	14	2.7	0.10
		$\frac{P_{vlbi}}{P_{tot}}$			4.7	0.03
q	vs.	P_{vlbi}	31	14	2.1	0.15
q	Vs.	$\frac{P_{vlbi}}{P_{tot}}$			0.8	0.36
q'	Vs.	P'_{vlbi}			3.8	0.05
q'	Vs.	$\frac{P_{vlbi}}{P_{tot}}$			2.4	0.12
M_{H_2}	Vs.	P_{vlbi}	27	13	4.0	0.05
		P'_{vlbi}			3.7	0.05
		$\frac{P_{vlbi}}{P_{tot}}$			0.71	0.40
IR/H_2	vs.	P_{vlbi}	27	13	0.14	0.71
		P'_{vlbi}			0.07	0.79
		$\frac{P_{vlbi}}{P_{tot}}$			0.45	0.50
M_{H_2}	Vs.	L_{FIR}	34	0	6.5	0.01
L_{FIR}	vs.	P_{tot}	40	0	17.6	<10-4
		P'_{tot}			58.9	<< 10-4
L_{FIR}	Vs.	q	40	0	3.8	0.05
	Vs.	q'			1.2	0.28
L_{FIR}	Vs.	[25/60]	40	0	0.5	0.49
L_{FIR}	Vs.	[60/100]	40	0	10.8	0.001
L_{FIR}	vs.	$\alpha_{1.49}^{8.44}$	37	0	6.2	0.01

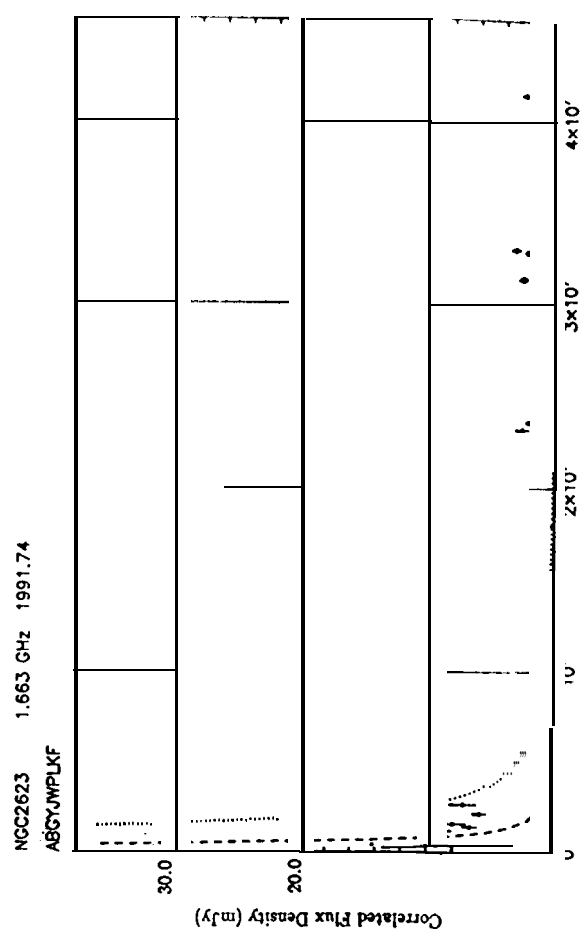
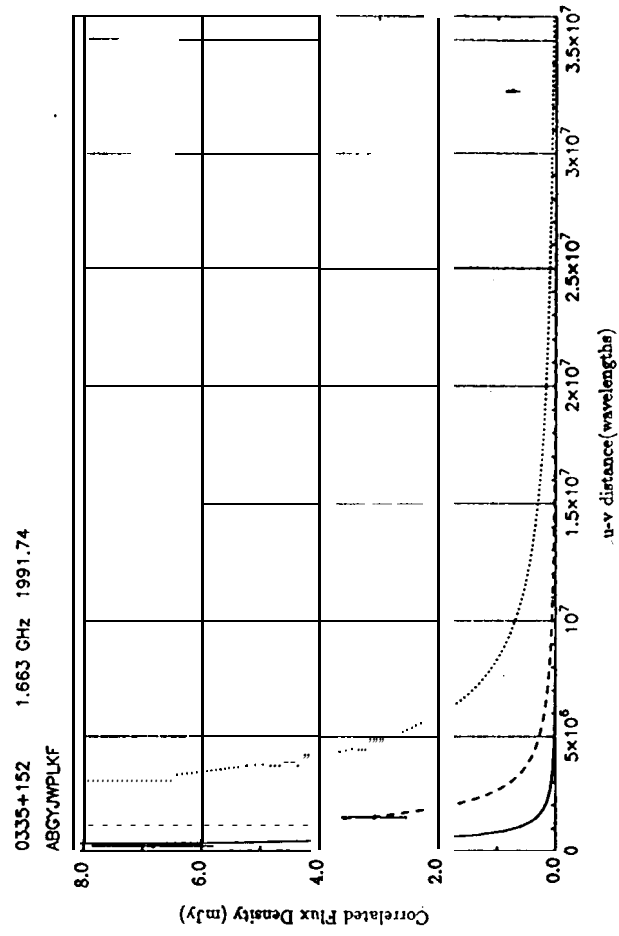
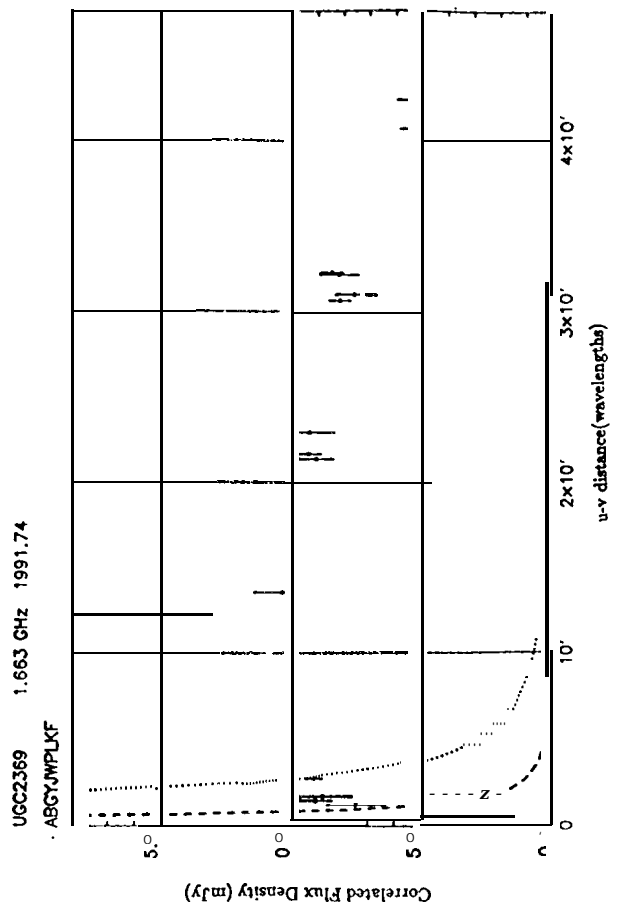
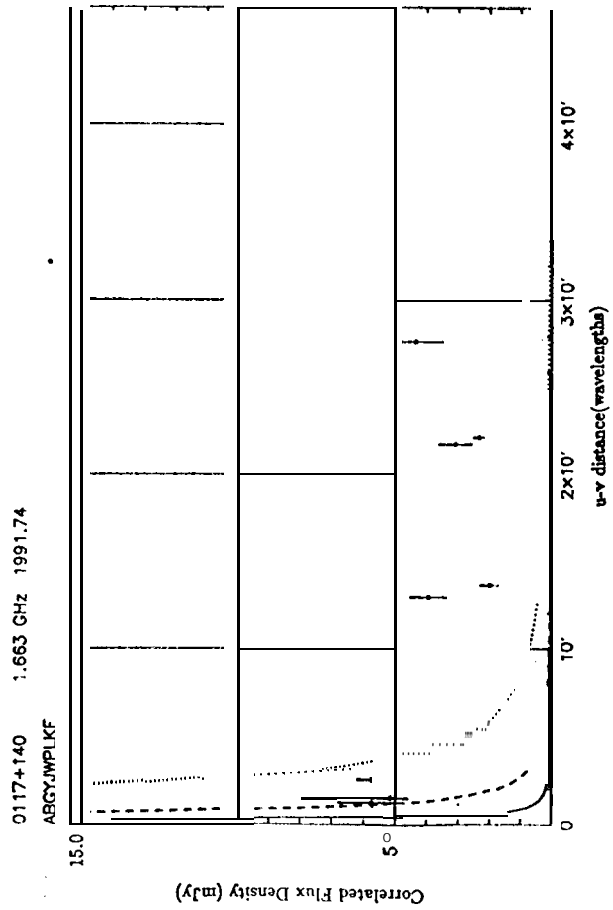
TABLE 5

LUMINOUS FIR GALAXY STARBURST MODELS

SYSTEM	L_{FIR}	P_{nt}^{ν} Observed	$P_{1.49}$	q	τ_{ff}	$P'_{1.49}$ Corrected	$P'_{1.49}$	q'	$L_{H\alpha}$	SFR	P_{nt}	ν_{SN} Model	$L_{H\alpha}$	Q^*
(1)	(2)	(3)	(4)	(5)	(6)	(7)	(8)	(9)	(10)	(11)	(12)	(13)	(14)	(15)
Model 1:	$m_l = 1M_{\odot};$		$m_u = 45M_{\odot};$			$t_{bb} = 10^{8.0}yr;$			$m_{SN} = 8M_{\odot}$					
	$< P_{nt}/P_{ff} > = 25$	$Q = 1.5GHz;$		$q = 2.35;$		$log(M/L) = -2.59(M_{\odot}/L_{\odot})$								
Mrk 938	11.28	<21.25	22.62	2.62	0.00	<21.26	22.62	2.52	42.93	16.14	22.80	0.26	42.01	...
IC 1623	11.99	<21.45	23.11	2.14	0.00	<21.45	23.11	2.14	41.90	20.80	22.91	0.33	42.12	9.12
01076-1707	11.42	<21.39	22.93	2.35	0.00	<21.39	22.93	2.35	42.48	22.28	22.94	0.36	42.15	
01173+1405	11.64	22.11	22.90	2.46	0.00	22.11	22.90	2.46	42.02	29.38	23.06	0.47	42.27	...
01364-1042	11.67	<21.92	22.85	2.67	0.49	<22.13	23.06	2.46	41.22	39.63	23.19	0.63	42.40	
111 Zw 35	11.46	<21.15	22.74	2.57	0.52	<21.37	22.97	2.34	41.45	24.43	22.98	0.39	42.19	8.45
NGC 695	11.51	<21.38	23.13	2.22	0.00	<21.38	23.13	2.22	41.88	27.42	23.03	0.44	42.24	8.90
UGC 2369	11.42	22.44	22.89	2.38	0.05	22.46	22.91	2.36	42.26	22.28	22.94	0.36	42.15	
03359+1523	11.37	21.85	22.64	2.58	0.68	22.14	22.94	2.29	41.97	19.86	22.89	0.32	42.10	9.07
04191-1855	11.34	<21.65	22.69	2.49	0.09	<21.69	22.73	2.45	41.80	18.54	22.86	0.30	42.07	
NGC 1614	11.39		22.67	2.58	0.00		22.67	2.58	42.67	20.80	22.91	0.33	42.12	8.71
05189-2524	11.91	<21.99	22.96	2.76	0.31	<22.13	23.10	2.62	42.94	68.87	23.43	1.10	42.64	8.53
NGC 2623	11.47	21.79	22.83	2.50	0.21	21.88	22.92	2.41	...	25.00	22.99	0.40	42.20	8.37
08572+3915	11.96	<22.00	22.63	3.10	0.75	<22.32	22.96	2.73	41.29	77.27	23.48	1.24	42.69	
UGC 4881	11.61	22.10	22.96	2.49	0.02	22.11	22.97	2.48	42.70	34.51	23.13	0.55	42.34	8.92
UGC 5101	11.93	22.95	23.67	2.10	0.19	23.04	23.75	2.02	43.10	72.11	23.45	1.15	42.66	
10173+0828	11.70	22.21	22.59	2.91	0.73	22.52	22.91	2.59	...	42.46	23.22	0.68	42.43	8.72
10566+2448	11.90	<22.43	23.20	2.55	0.03	<22.44	23.22	2.53	43.05	67.30	23.42	1.08	42.63	8.51
11010+4107	11.62	<21.56	22.83	2.54	0.26	<21.67	22.94	2.43	...	28.05	23.04	0.45	42.25	8.73
UGC 6436	11.44	<21.94	22.71	2.57	0.00	<21.94	22.71	2.57	42.97	23.33	22.96	0.37	42.17	...
Mrk 171	11.74	20.61	23.26	2.34	0.05	20.64	23.28	2.32	...	46.56	23.26	0.75	42.47	8.39
12112+0305	12.18	<22.12	23.36	2.66	0.40	<22.29	23.53	2.49	...	128.23	23.70	2.05	42.91	8.51
Mrk 231	12.35	23.61	23.93	2.23	...	23.61	23.93	2.23	42.30	189.67	23.87	3.04	43.08	7.91
Arp 238	11.62	<21.48	23.01	2.45	0.10	<21.52	23.06	2.40	42.42	35.32	23.14	0.57	42.35	8.58
13183+3424	11.81	<21.00	23.07	2.28	0.10	<21.05	23.12	2.23	41.82	27.42	23.03	0.44	42.24	8.43
Mrk 266	11.94	21.86	23.20	1.99	0.10	21.90	23.24	1.94	41.94	18.54	22.86	0.30	42.07	8.88
NGC 5257/8	11.37	<21.11	22.71	2.51	0.00	<21.11	22.71	2.51	40.65	19.86	22.89	0.32	42.10	...
Mrk 273	12.04	22.67	23.58	2.31	0.12	22.73	23.64	2.26	42.37	92.90	23.56	1.49	42.77	8.27
14348-1447	12.17	<22.50	23.62	2.37	0.00	<22.50	23.62	2.37	42.80	125.31	23.69	2.01	42.90	8.68
UGC 9618	11.58	<21.64	23.20	2.19	0.17	<21.72	23.28	2.11	40.94	32.21	23.10	0.52	42.31	
Mrk 848	11.72	22.06	23.19	2.38	0.00	22.06	23.19	2.38	42.69	44.46	23.24	0.71	42.45	8.62
15250+3608	11.88	22.57	22.86	2.80	1.02	23.01	23.31	2.36	41.82	64.27	23.40	1.03	42.61	
Arp 220	12.11	21.88	23.34	2.62	0.50	22.10	23.56	2.40	42.30	109.14	23.63	1.75	42.84	8.24
NGC 6090	11.33	<21.33	22.93	2.25	0.00	<21.33	22.93	2.25	42.40	18.11	22.85	0.29	42.06	8.89
NGC 6286	11.27	22.00	23.04	2.05	0.00	22.00	23.04	2.05	40.91	15.78	22.79	0.25	42.00	8.77
17132+5313	11.79	<21.89	23.16	2.46	0.05	<21.91	23.19	2.44	41.69	52.24	23.31	0.84	42.52	8.83
22491-1808	12.02	<22.64	22.82	2.90	0.50	<22.86	23.04	2.68	42.29	88.72	23.54	1.42	42.75	8.48
NGC 7469	11.41	21.79	22.98	2.29	0.03	21.81	23.00	2.27	42.17	21.78	22.93	0.35	42.14	8.62
Zw 475.056	11.37	<21.07	22.58	2.64	0.05	<21.09	22.60	2.62	42.02	19.86	22.89	0.32	42.10	8.68
Mrk 331	11.27	21.67	22.62	2.51	0.07	21.70	22.65	2.48	42.15	15.78	22.79	0.25	42.00	8.91
n	40	17	40	40	39	17	40	39	35	40	40	40	35	28
< 1 >	11.63	22.13	23.00	2.47	0.20	22.22	23.08	2.39	42.12	36.35	23.15	0.58	42.35	8.63
Model 2:	$m_l = 8M_{\odot};$		$m_u = 45M_{\odot};$			$t_{bb} = 10^{8.0}yr;$			$m_{SN} = 8M_{\odot}$					
	$< P_{nt}/P_{ff} > = 25$	$Q = 1.5GHz;$		$q = 2.35;$		$log(M/L) = -2.59(M_{\odot}/L_{\odot})$								
< 2 >										11.58	23.15	0.77	42.35	9.13
Model 3:	$m_l = 0.1M_{\odot};$		$m_u = 60M_{\odot};$			$t_{bb} = 10^{8.0}yr;$			$m_{SN} = 8M_{\odot}$					
	$< P_{nt}/P_{ff} > = 160$	$Q = 1.5GHz;$		$q = 2.33;$		$log(M/L) = -1.91(M_{\odot}/L_{\odot})$								
< 3 >										55.50	23.16	0.50	42.55	8.45
LH Model:	$m_l = 1M_{\odot};$		$m_u = 100M_{\odot};$			$t_{bb} = 10^{8.0}yr;$			$m_{SN} = 8M_{\odot}$					
	$< P_{nt}/P_{ff} > = 12.5$	$Q = 1.5GHz;$		$q = 2.34$										
< LH >										23.67	23.15	0.47	43.055	8.81

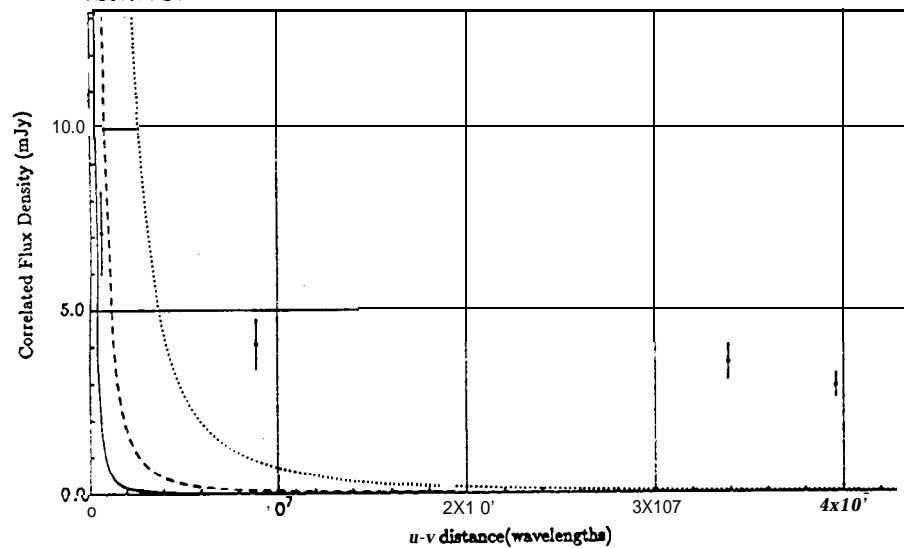
TABLE 6
STARBURST/RSN VISIBILITY FUNCTION MODELS

source	$S_{\nu lbi}$ (mJy)	ν_{sn}^{fir} (W - ')	$S_{\nu lbi}^{gauss}$ (mJy)	P_{sn}^{1986J}	ν_{sn}^{gauss} (yr^{-1})	SN Ratio	fit	$S_{\nu lbi}^{clump}$ (mJy)	P_{sn}^{1986J}	ν_{sn}^{clump} (yr^{-1})	SN Ratio	P_{cl}^{1986J}	N_{cl}	$\frac{N_{rsn}}{N_{cl}}$	d_{cl} (pc)	fit		
(1)	(2)	(3)	(4)	(5)	(6)	(7)	(8)	(9)	(10)	(11)	(12)	(13)	(14)	(15)	(16)	(17)		
gaussian models								clumped models										
01173+1405	7.0	0.47	3.0	2.8	0.54	1.15	m	3.0	4.0	0.49	1.05	12	1.6	3	5	a		
UGC 2369	15.0	0.44	8.0	16.0	0.13	0.30	p	6.0	25.0	0.08	0.18	50	0.4	2	1	1.		
NGC 2623	9.0	0.40	3.0	0.7	1.10	2.75	p	3.0	4.0	0.15	0.38	16	0.4	4	4	l		
UGC 4881	4.0	0.55	4.0	8.0	0.35	0.63	ml	3.5	8.0	0.31	0.56	16	1.5	2	4	a		
UGC 5101	28.0	1.15	3.0	2.8	1.43	1.24	p	3.0	5.0	0.94	0.82	100	0.5	20	4	p		
Mrk 231	115.	3.04	25.0	16.0	4.20	1.38	p	20.0	30.0	0.91	0.30	300	0.9	10	2	a		
Mrk 273	16.0	1.49	4.0	2.8	2.38	1.60	p	4.0	3.3	1.98	1.33	20	3.3	6	10	a		
Arp 220	10.5	1.75	6.0	1.0	2.71	1.55	m	4.0	1.0	2.32	1.33	12	1.9	12	10	a		
NGC 6286	13.0	0.25	8.0	16.0	0.04	0.16	m	8.0	5.0	0.39	1.57	20	1.0	4	15	1'		
NGC 7469	12.0	0.35	3.0	1.0	0.41	1.16	p	3.0	1.7	0.33	0.94	1	0	0	5	6	2	a
Mrk 331	7.5	0.25	4.0	1.4	0.34	1.34	m	3.0	2.0	0.26	1.04	6	0.9	3	1	a		



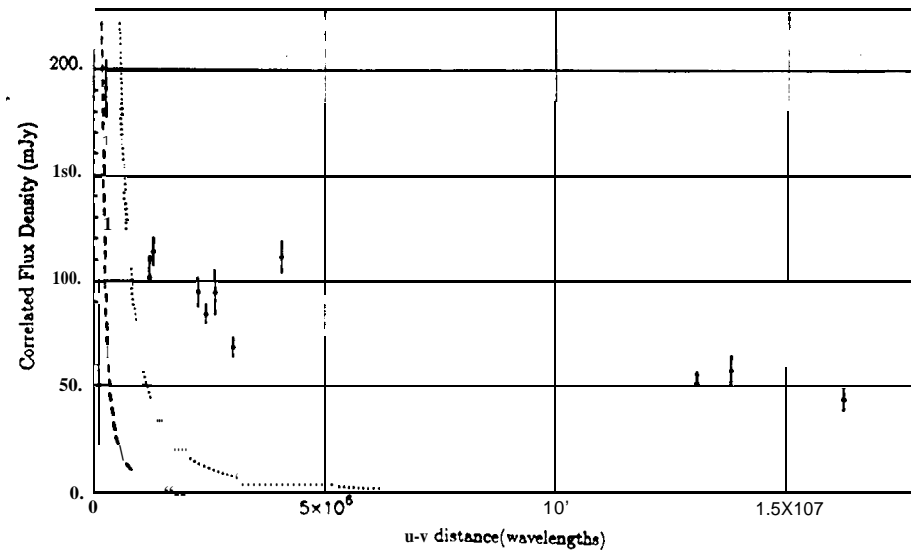
UGC4881 1.663 GHz 1991.74

ABGYJWPLKF



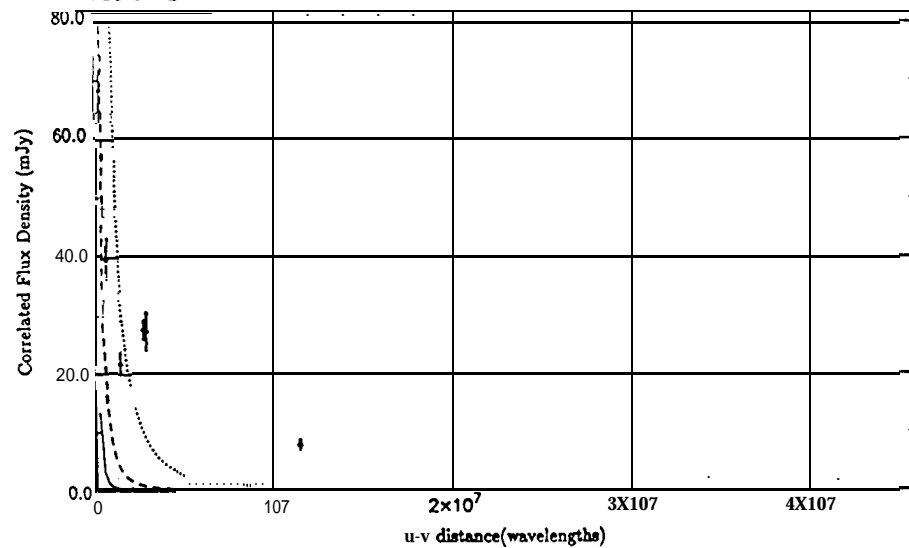
MRK231 1.667 GHz 1991.74

ABGYJWPLKF



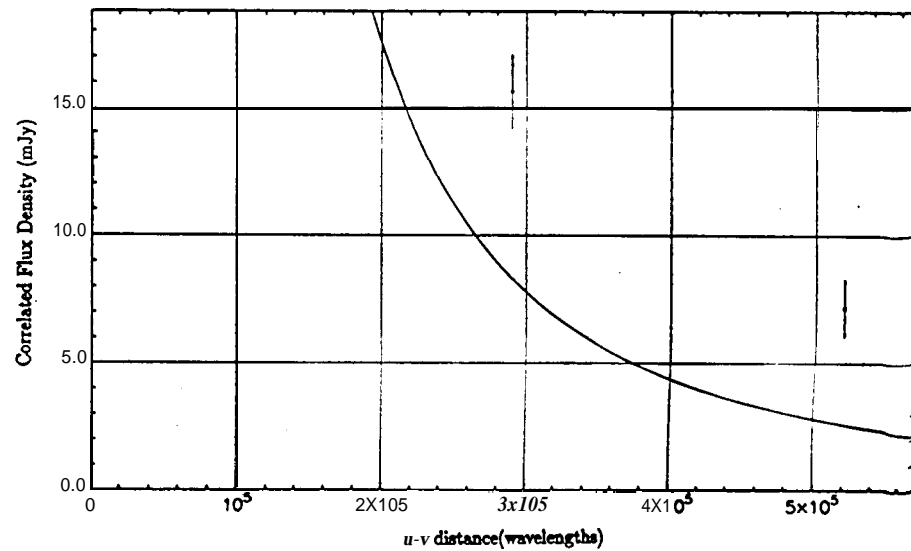
UGC5101 1.663 GHz 1991.74

ABGYJWPLKF

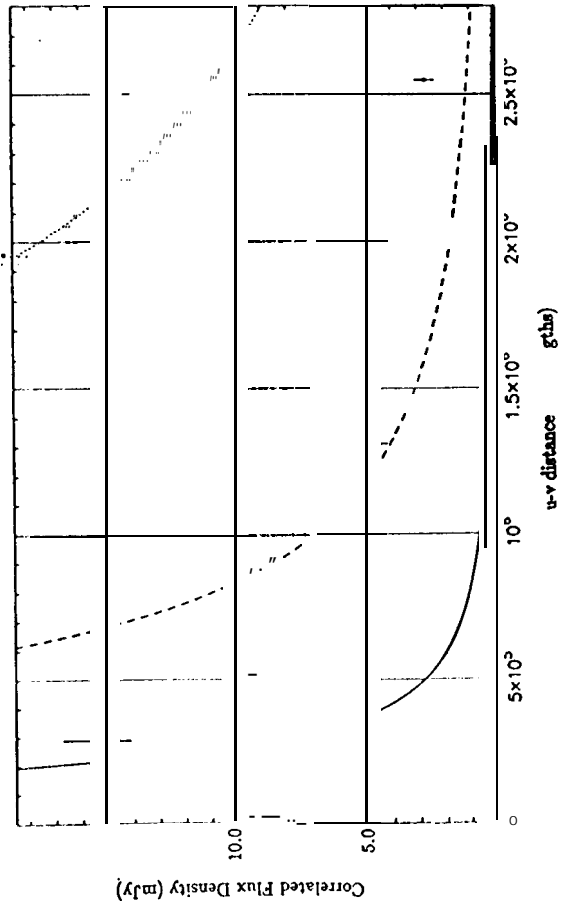


MRK171D 1.667 GHz 1991.74

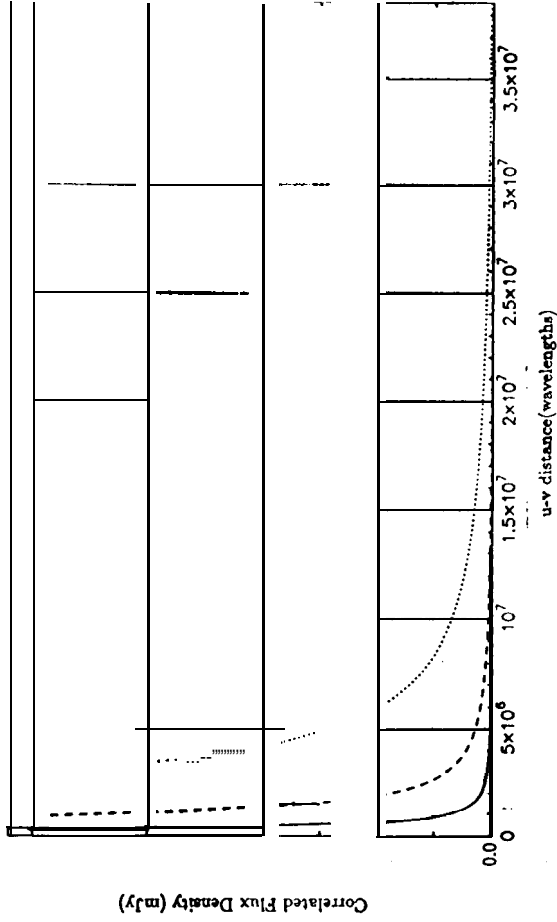
ABGYJWPLKF



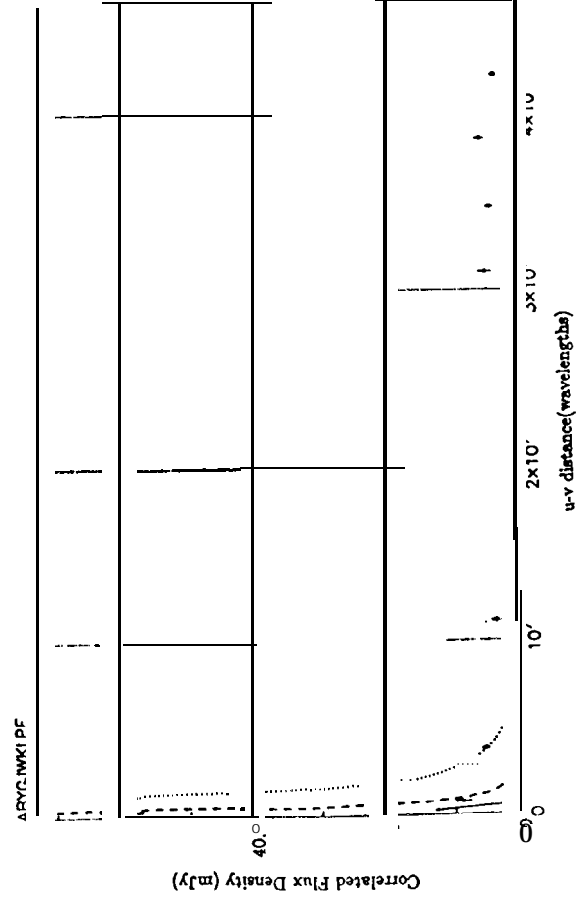
MRK266 1.663 GHz 1991.74



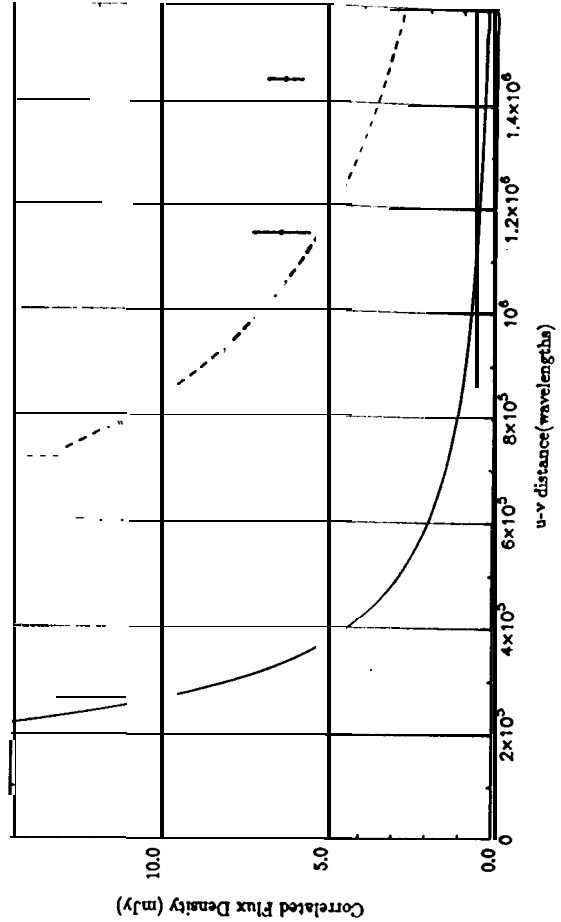
MRK848 1.663 GHz 1991.74
ABGYJWPLKF

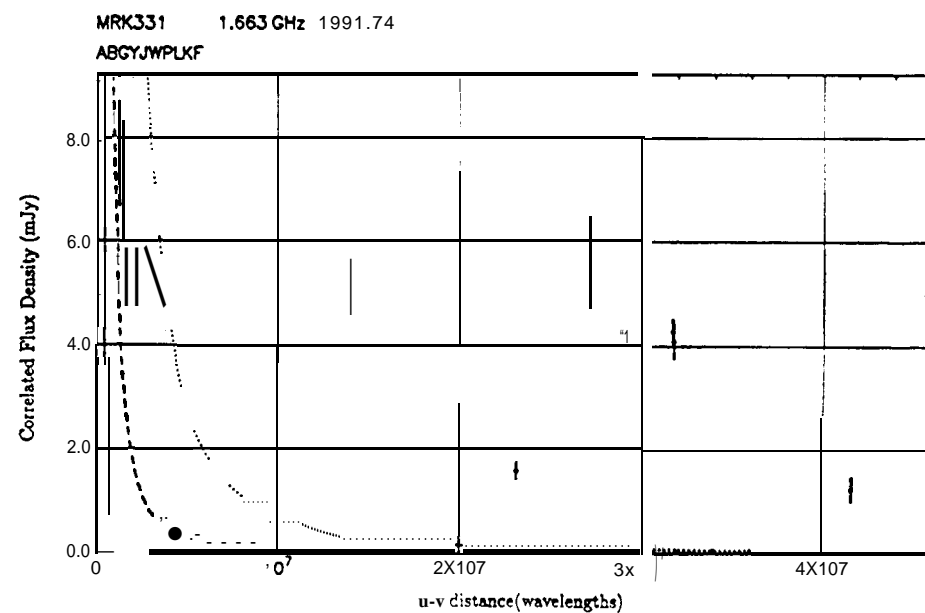
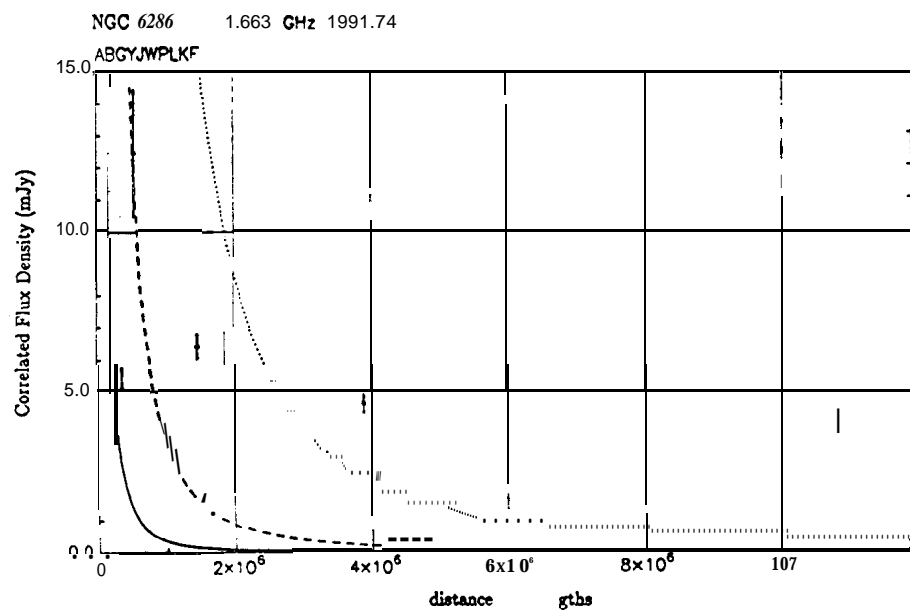
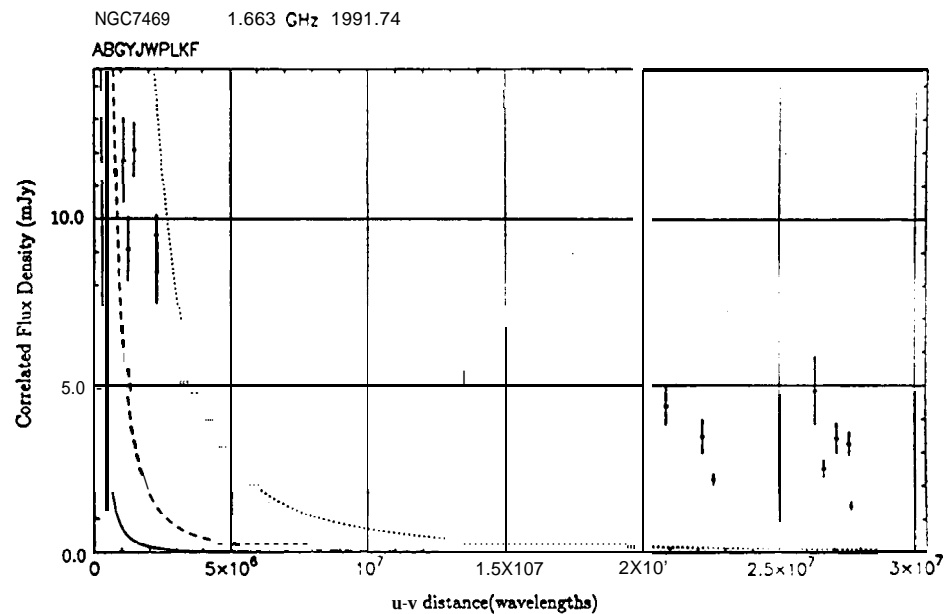
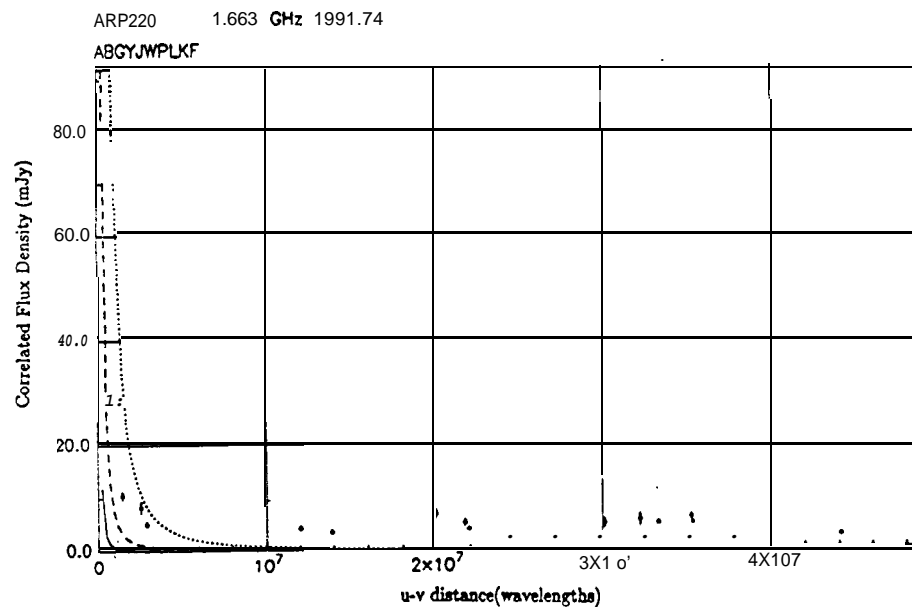


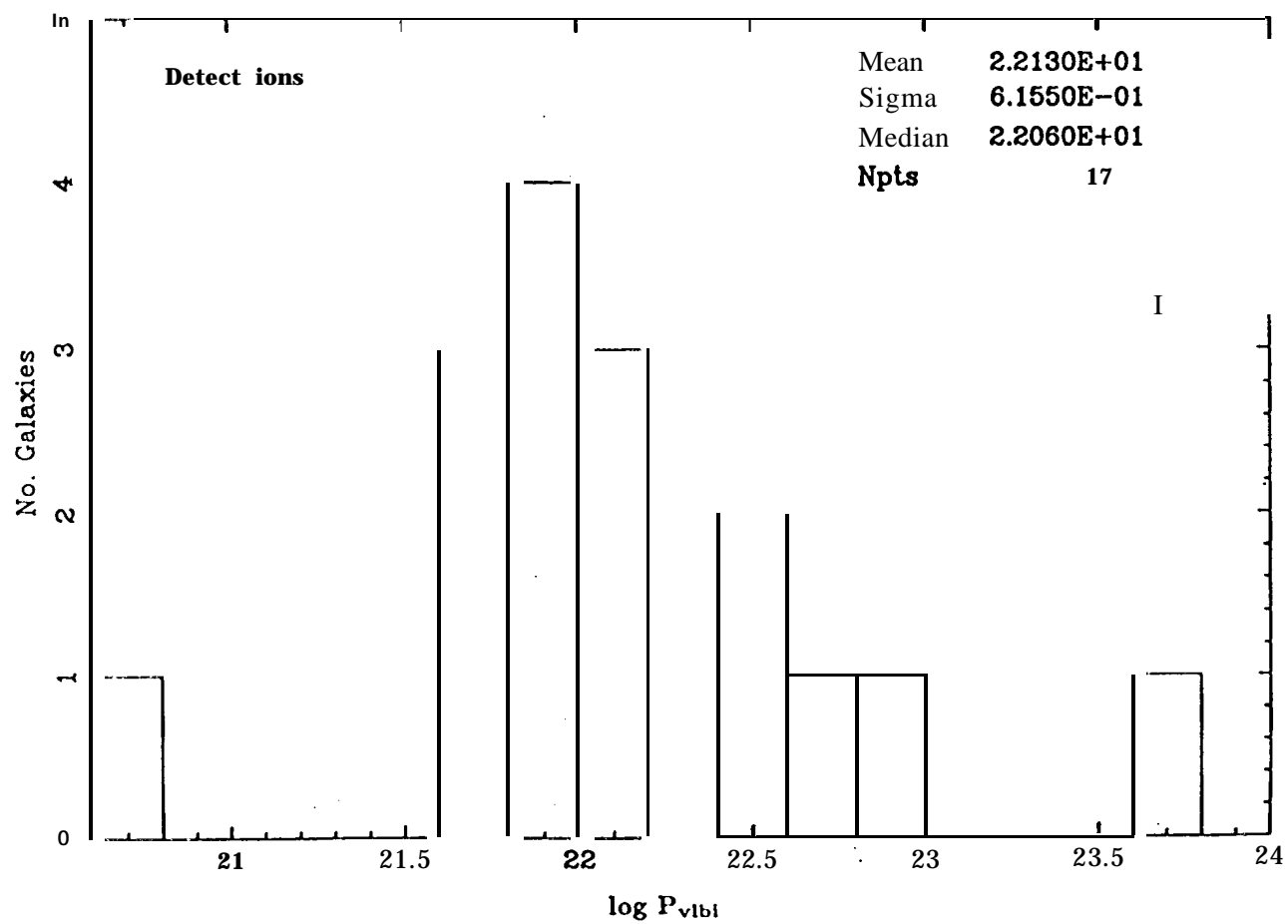
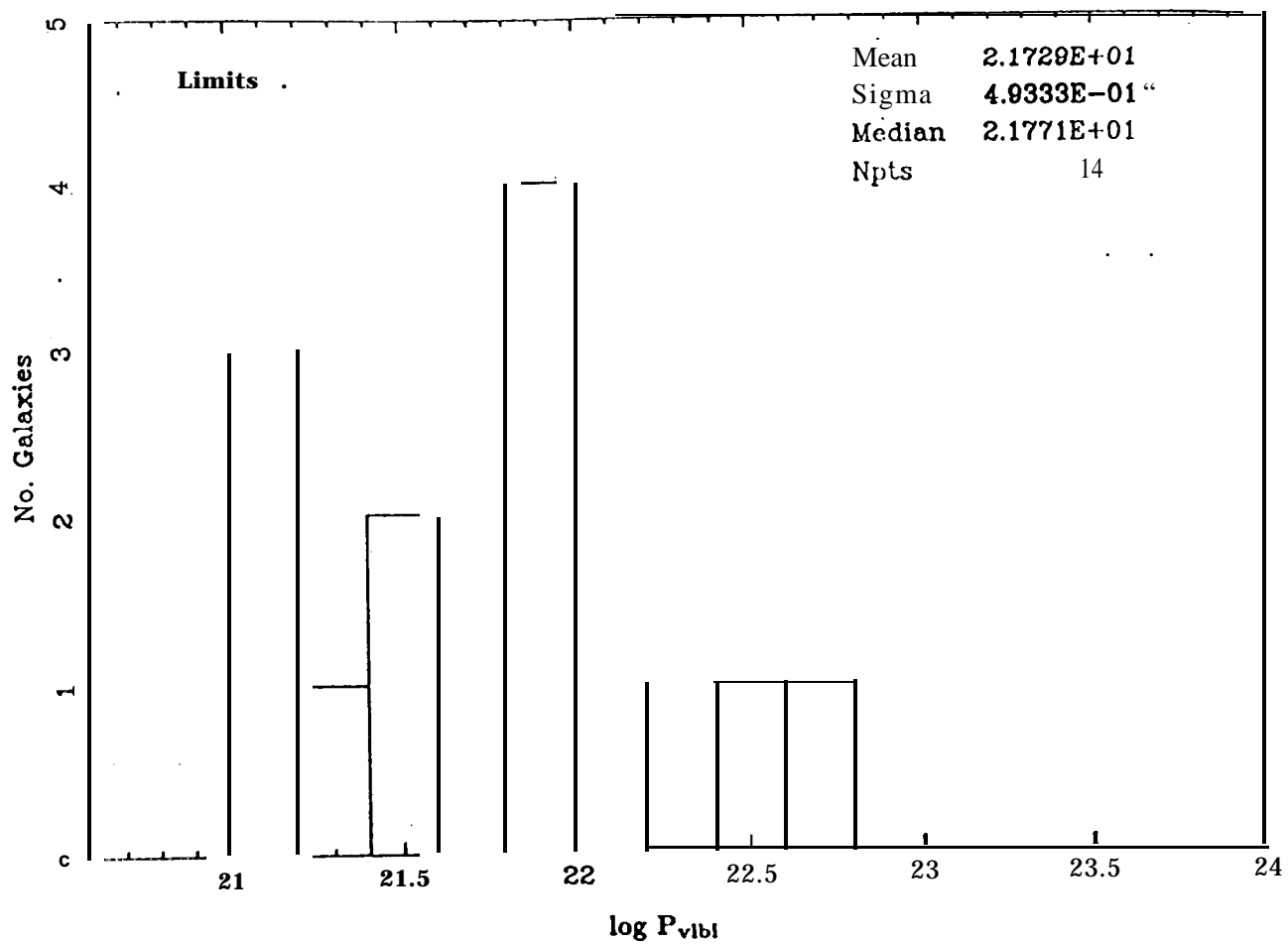
MRK273 1.663 GHz 1991.74

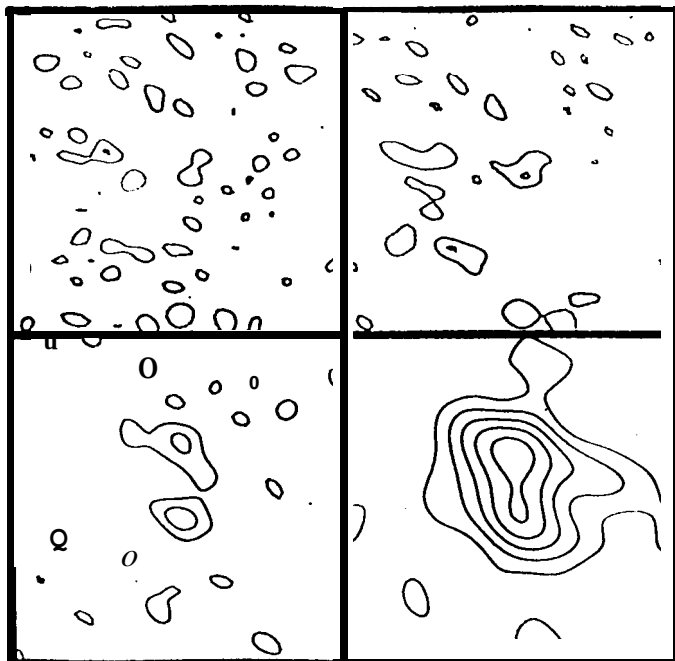


1525+36^s 1.663 GHz 991.74
ABGYJWPLKF



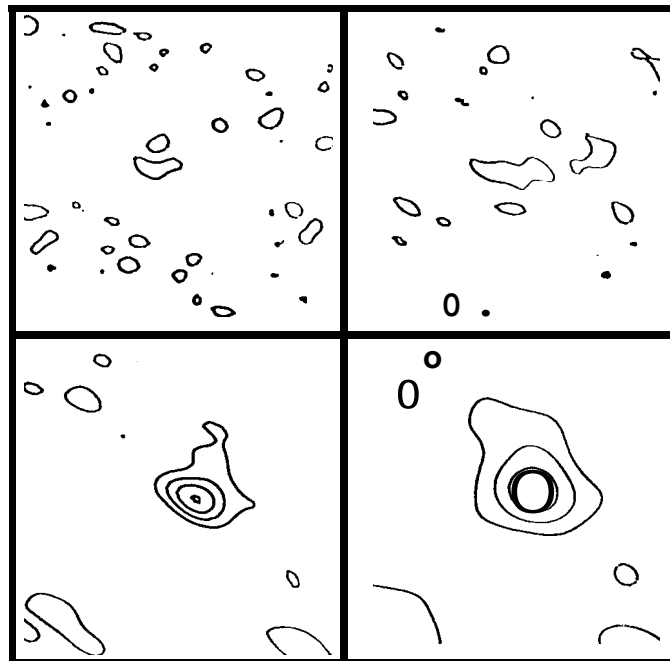






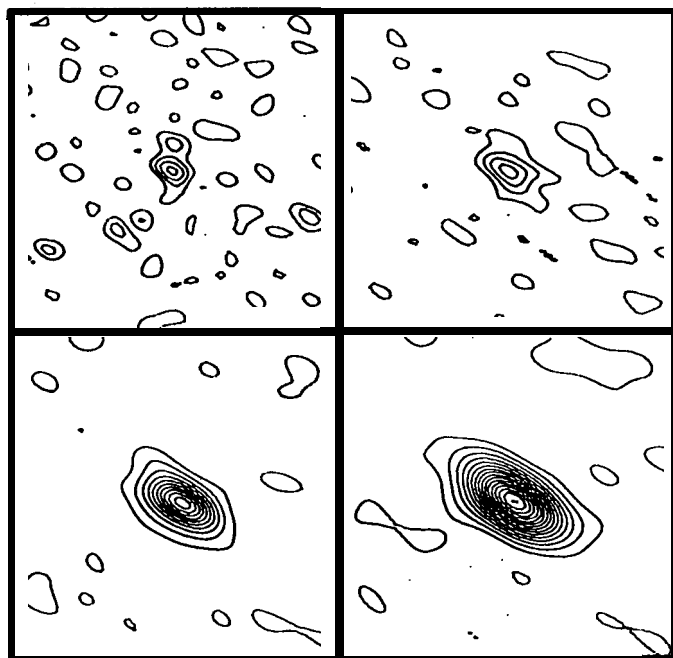
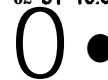
22GHz uniform 122 x 86,66" C.I. 0.8mJy	22GHz Natural 177 X105,60" C.I. 0.5mJy
15GHz uniform 199x117,61" C.I. 0.5mJy	15GHz Tapered 349 x 249,80" C.I. 0.3mJy

0117+140
Field center at:
01°17'23.170, +14°05'58.68



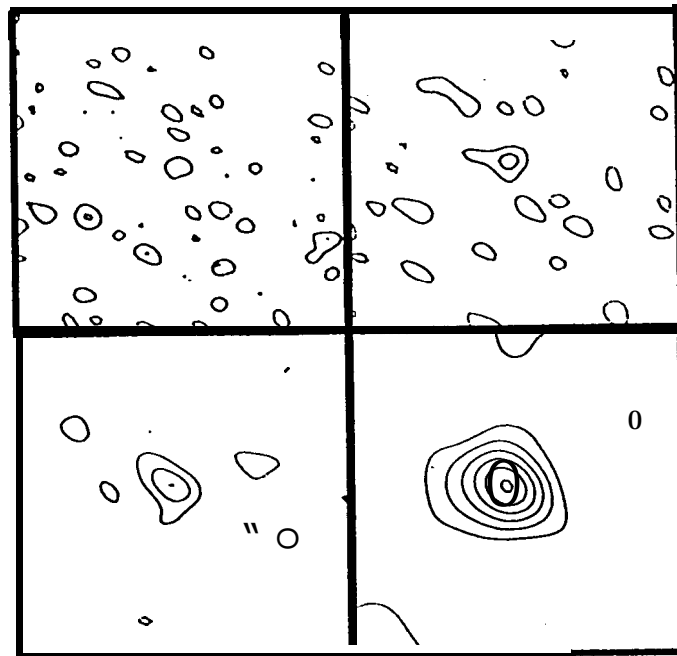
22GHz Uniform 111 x 86, 67" C.I. 1.0mJy	22GHz Natural 159 x 106, 60" C.I. 0.6mJy
15GHz Natural 259 x 147,59" C.I. 0.4mJy	15GHz Tapered 340 x 249,60" C.I. 0.4mJy

UGC 2369
Field center at:
02°51'15.938, +14°46'04.00



22GHz Uniform 137 x 89, 65" C.I. 1.0mJy	22GHz Natural 164x105,62" C.I. 0.6mJy
15GHz Uniform 245 X 117,62" C.I. 0.7mJy	15GHz Natural 300 x 143,61" C.I. 0.5mJy

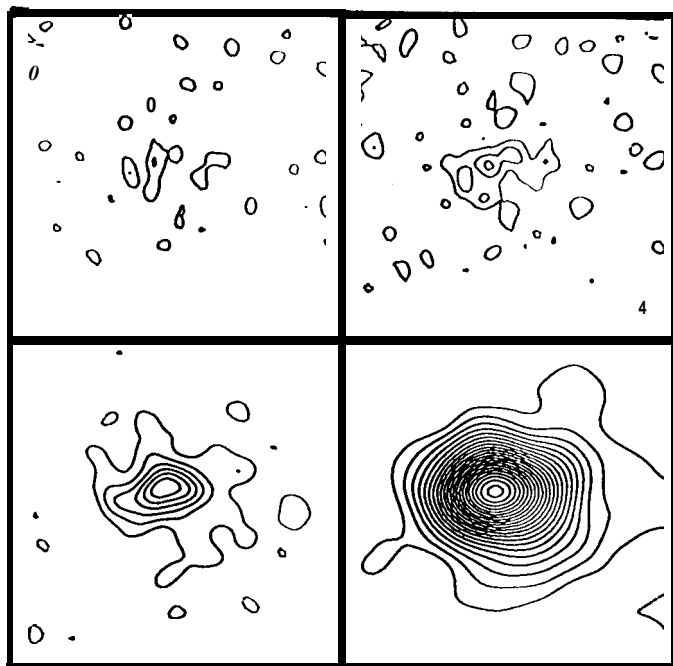
III Zw 035
Field center at:
01°41'47.920, +16°51'06.28



22GHz Uniform 120 x 85, 66" C.I. 0.8mJy	22GHz Natural 169 x 105, 61" C.I. 0.5mJy
15GHz Uniform 197x114,602" C.I. 0.7mJy	15GHz Tapered 353 x 246,80" C.I. 0.4mJy

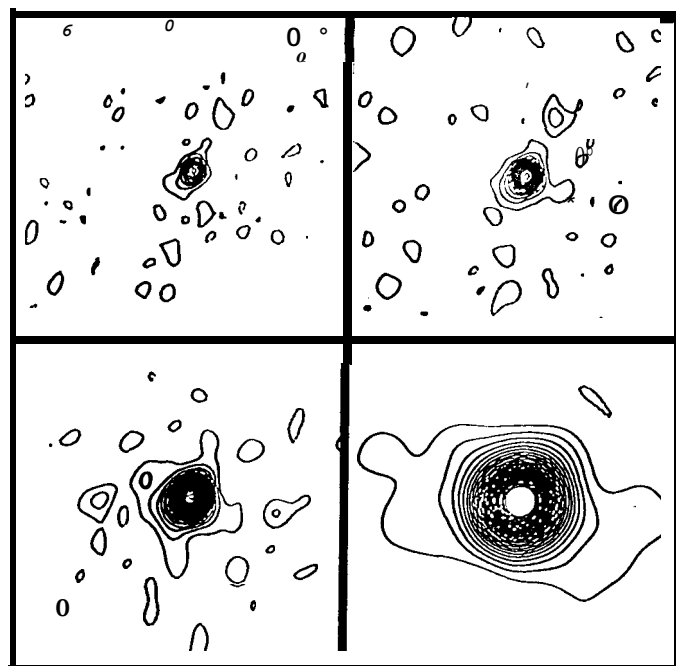
0335+152
Field center at
03°35'58.334, +15°23'09.38





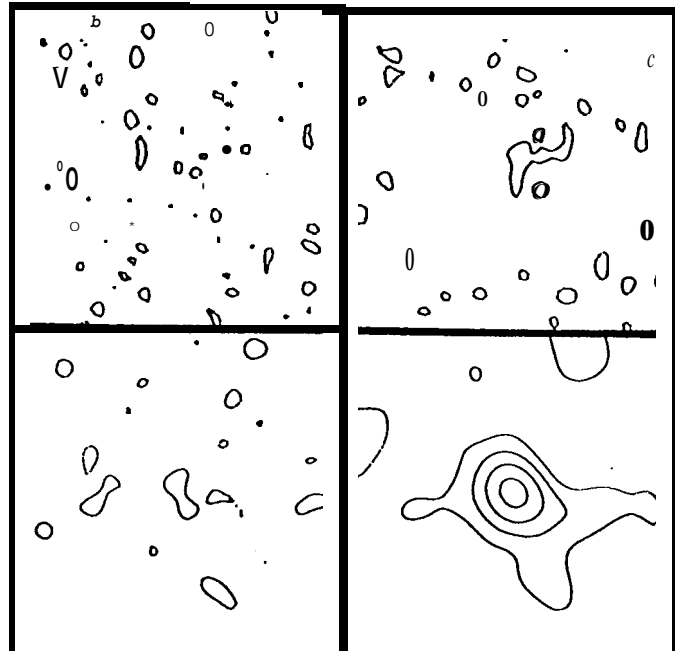
22GHz Uniform 85 x 72, 1" Cl. 1.0mJy	22GHz Natural 103 x 88, -7" C.I. 0.7mJy
15GHz Uniform 125x119, 8" Cl. 0.6mJy	15GHz Tapered 267 X 257, -57" C.I. 0.4mJy

NGC 2623
Field center at:
08°35'57.0" +25° 55' 50.18"



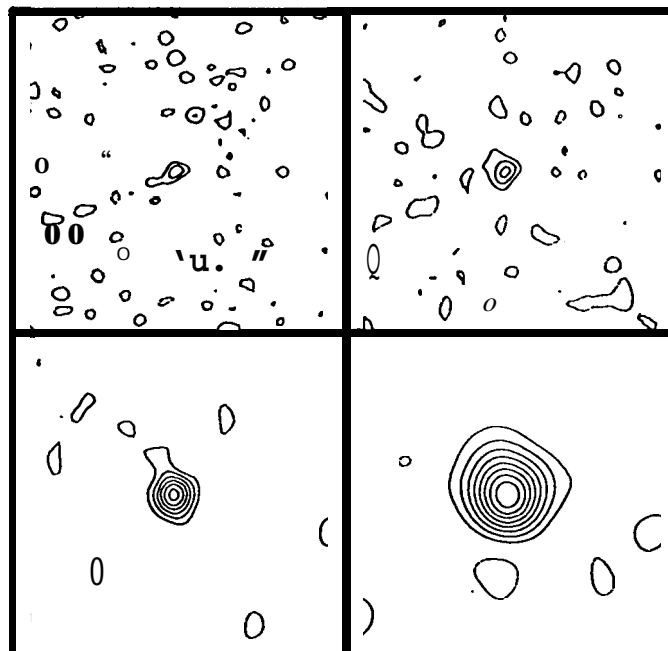
22GHz Uniform 93X 69, -7" Cl. 1.0mJy	22GHz Natural 111x88, -9" C.I. 0.7mJy
15GHz Uniform 141 x 113, -14" Cl. 0.7mJy	15GHz Tapered 272 X 259, -32" Cl. 0.7mJy

UGC 5101
Field center at:
09°32'04.780" +61° 34'36.90"



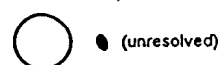
22GHz Uniform 77 X 67, 0" Cl. 0.8mJy	22GHz Natural 100 X 87, -11" Cl. 0.5mJy
15GHz Uniform 118X104, -6" Cl. 0.6mJy	15GHz Tapered 267 X 258, -54" Cl. 0.4mJy

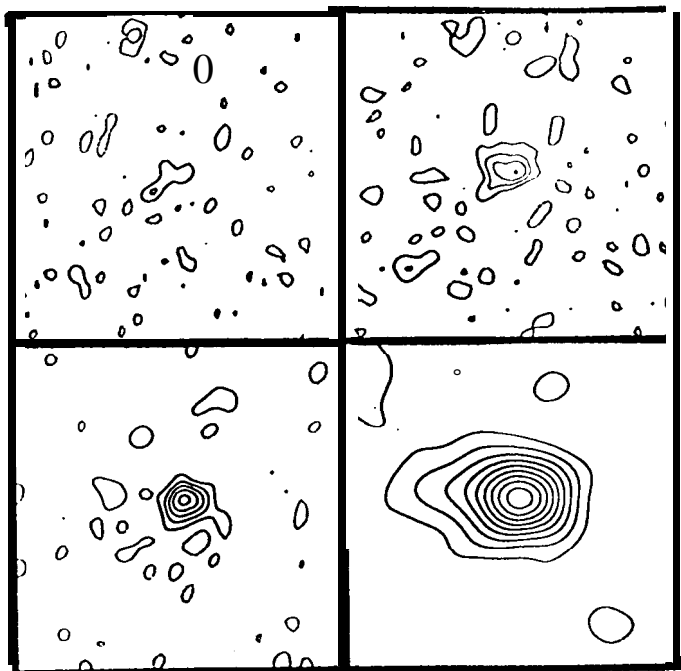
UGC 4881
Field center at:
09°12'38.430" +44° 32' 29.18"



22GHz Uniform 80x 74, -26" C.I. 0.8mJy	22GHz Natural 110X89, -2" Cl. 0.5mJy
15GHz Uniform 125x114, -16" C.I. 0.5mJy	15GHz Tapered 266 X 258, -13" Cl. 0.4mJy

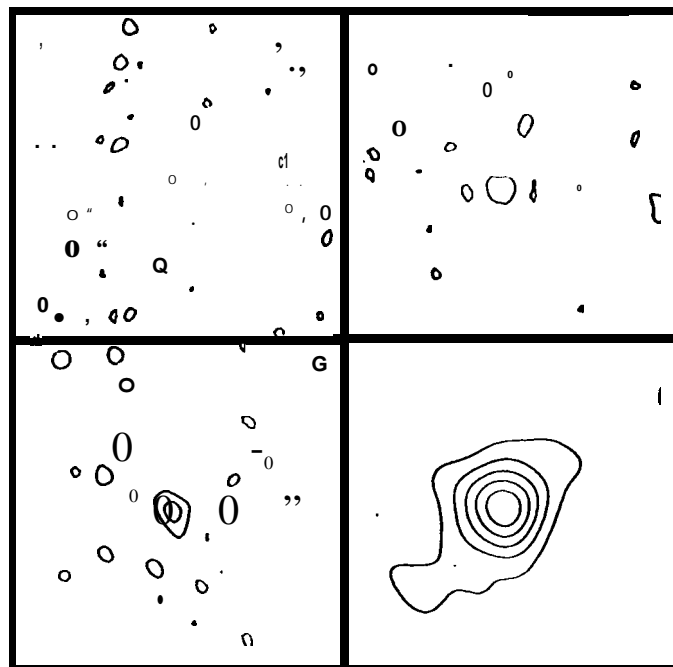
1017+082
Field center at
10°17'25.7" +08° 28' 39.4"





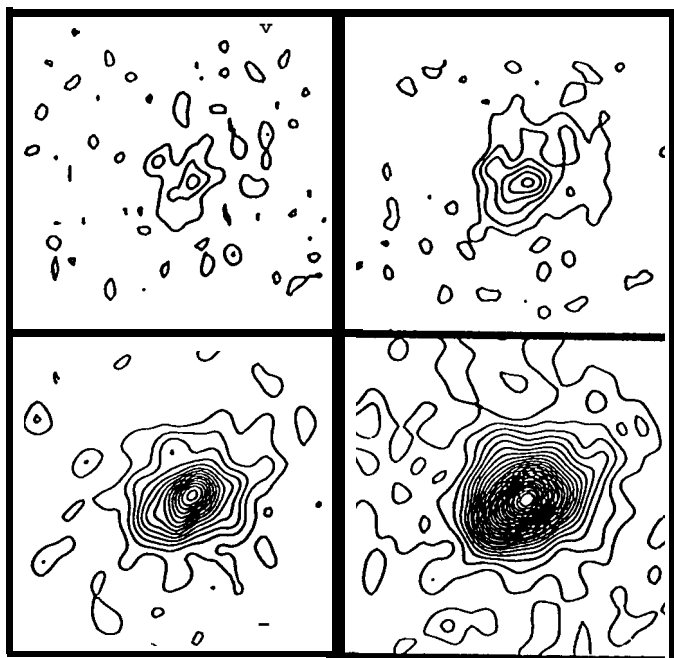
22GHz Uniform 82 x 69, -27" C.I. 0.8mJy	22GHz Natural 100 x 91, -24" C.I. 0.5mJy
15GHz Uniform 123 x 103, -34" Cl. 0.5mJy	15GHz Tapered 269 x 257, -78" Cl. 0.4mJy

1101+410
Field center at:
11^h 01^m 05^s.810, +41° 07' 10".48



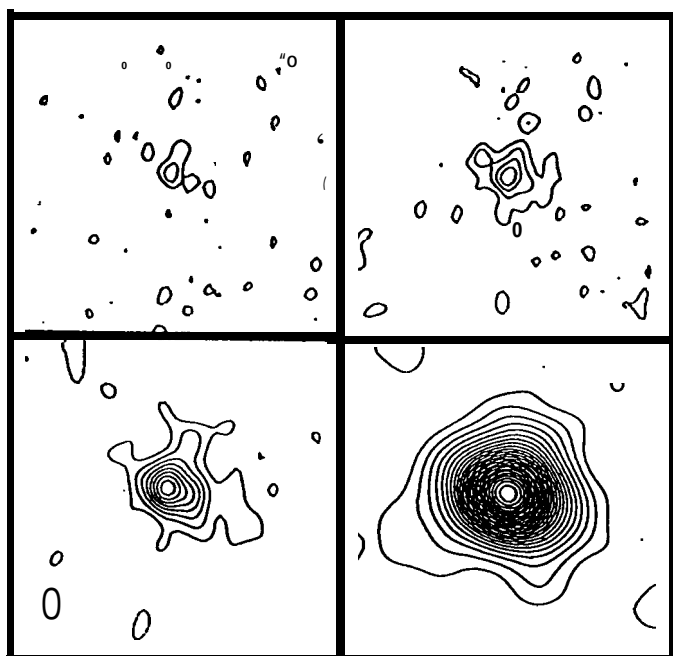
22GHz Uniform 79X 67, -5" C.I. 1.0mJy	22GHz Natural 102 X 69, -6" C.I. 0.7mJy
15GHz Uniform 119x102, -8" Cl. 0.6mJy	15GHz Tapered 267 x 259, -55" Cl. 0.4mJy

MRK 266
Field center at:
13^h 36-15:010, +46° 31' 54".08



22GHz Uniform 89X 68, -3" C.I. 1.3mJy	22GHz Natural 109 x 88, -4" Cl. 1.0mJy
15GHz Uniform 137X 114, -9" Cl. 0.8mJy	15GHz Natural 162 x 139, -8" Cl. 0.5mJy

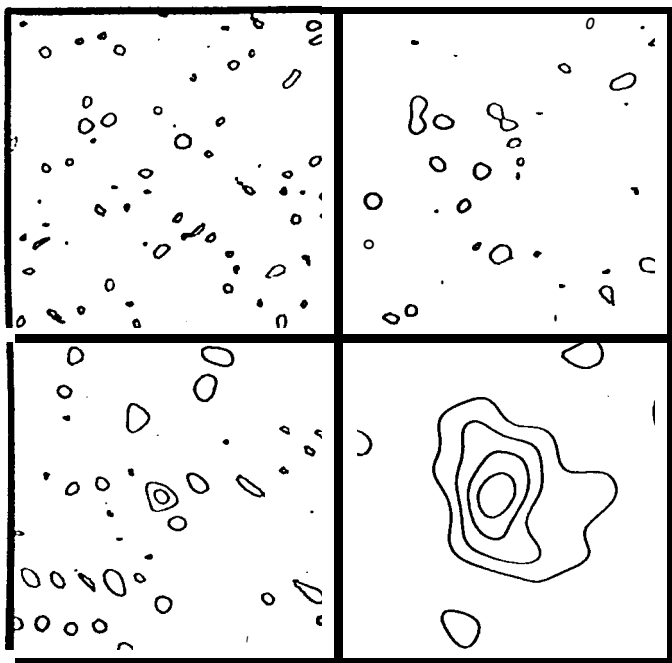
MRK 171D
Field center at:
11^h 25^m 44^s.190, +58° 60' 18".18



22GHz Uniform 90X70, -17" Cl. 1.2mJy	22GHz Natural 107 X 89, -14" C.I. 0.8mJy
15GHz Uniform 139 x 115, -19" C.I. 0.8mJy	15GHz Tapered 270 x 258, -48" C.I. 0.5mJy

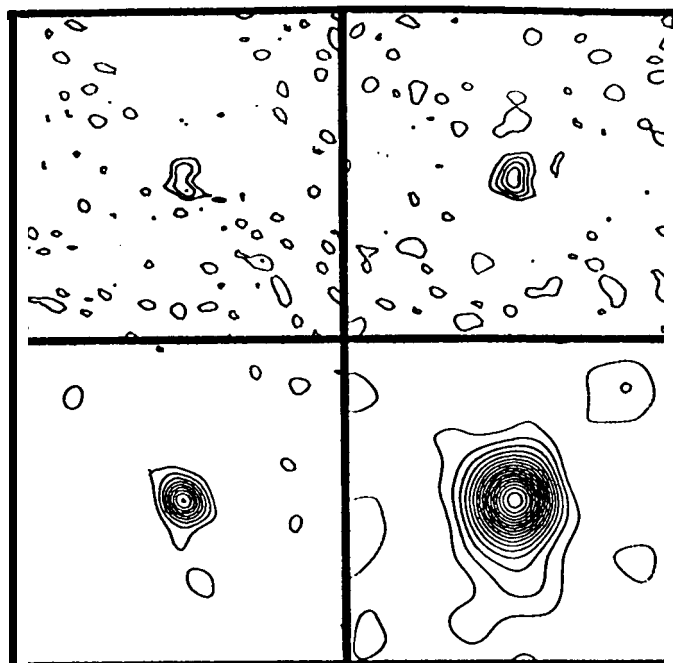
MRK 273
Field center at:
13^h 42^m 14^s.0, +56° 08' 14".28





22GHz Uniform 78X 67,4' C.I. 1.2mJy	22GHz Natural 100X88, -4" C.I. 0.8mJy
15GHz Uniform 118x 103, 1° C.I. 0.7mJy	15GHz Tapered 286 x 258, -59" C.I. 0.4mJy

MRK 848
Field center at
15° 16' 19.291, +42° 55' 38.38



22GHz Uniform 89 x 75, 49° C.I. 1.0mJy	22GHz Natural 103 x 99, 86° C.I. 0.8mJy
15GHz Uniform 134 x 125, 54° C.I. 0.7mJy	15GHz Tapered 273 x 256, -64° C.I. 0.4mJy

1525+360
Field center at:
15° 25' 03.720, +36° 09' 00.98

